Nano Research

ISSN 1998-0124 CN 11-5974/O4
https://doi.org/10.26599/NR.2026.94909297

Research Article

Ni-induced interfacial engineering enables recycled aluminum hydride for high-efficiency electrochemical hydrogen storage

Man Liu[1], Chunqi Zhang[1], Licheng Liang[1], Chuan Cao[1], Yichen Li[4], Mingan Ren[4], Ning Wang[5], Qingshuang Wang[3](✉), Qingqing Yang[2](✉), Fei Liang[1](✉)

[1] Institutes of Physical Science and Information Technology, Anhui University, Hefei 230601, China

[2] School of Materials Science and Engineering, Anhui University, Hefei 230601, China

[3] School of Materials Science and Engineering, Changchun University of Science and Technology, Changchun 130022, China

[4] Henan Hydrogen Source Technology Co., Ltd., Xinxiang 453000, China

[5] School of Science, Key Laboratory of High Performance Scientific Computation, Xihua University, Chengdu 610039, China

Nano Res., **Just Accepted Manuscript** • https://doi.org/10.26599/NR.2026.94909297

https://www.sciopen.com/journal/1998-0124 on Oct. 30, 2026

© The Authors(s)

Just Accepted

This is a "Just Accepted" manuscript, which has been examined by the peer-review process and has been accepted for publication. A "Just Accepted" manuscript is published online shortly after its acceptance,which is prior to technical editing and formatting and author proofing. Tsinghua University Press (TUP) provides "Just Accepted" as an optional and free service which allows authors to make their results available to the research community as soon as possible after acceptance. After a manuscript has been technically edited and formatted, and the page proofs have been corrected, it will be removed from the "Just Accepted" web site and published officially with volume and article number (e.g., *Nano Research*, **2025**, *18*, 94906990). Please note that technical editing may introduce minor changes to the manuscript text and/or graphics which may affect the content, and all legal disclaimers that apply to the journal pertain. In no event shall TUP be held responsible for errors or consequences arising from the use of any information contained in these "Just Accepted" manuscripts. To cite this anuscript please use its Digital Object Identifier (DOI®),which is identical for all formats of publication.

Research Article

Ni-induced interfacial engineering enables recycled aluminum hydride for high-efficiency electrochemical hydrogen storage

Man Liu [1], Chunqi Zhang [1], Licheng Liang [1], Chuan Cao [1], Yichen Li [4], Mingan Ren [4], Ning Wang [5], Qingshuang Wang [3] ✉, Qingqing Yang [2] ✉, Fei Liang [1] ✉

[1] Institutes of Physical Science and Information Technology, Anhui University, Hefei 230601, China
[2] School of Materials Science and Engineering, Anhui University, Hefei 230601, China
[3] School of Materials Science and Engineering, Changchun University of Science and Technology, Changchun 130022, China
[4] Henan Hydrogen Source Technology Co., Ltd., Xinxiang 453000, China
[5] School of Science, Key Laboratory of High Performance Scientific Computation, Xihua University, Chengdu 610039, China

Received: 26 August 2026; **Revised: 5 October 2026**; **Accepted: 30 October 2026**

✉Address correspondence to Fei Liang, fliang@ahu.edu.cn; Qingqing Yang, qqyang@ahu.edu.cn; Qingshuang Wang, wangqingshuang@163.com

Cite this article: *Nano Research*, 2027, 20, 94909297 https://doi.org/10.26599/NR.2026.94909297

Just Accepted

ABSTRACT: Aluminum-based hydrides are attractive hydrogen carriers because of high gravimetric hydrogen capacity and relatively moderate working temperature. However, poor reversibility significantly increases the difficulty of application of aluminum hydride materials. Electrochemical hydrogen storage represents an attractive alternative for hydride synthesis and recycling which would be integrated with green electricity. In this work, a Ni-induced interfacial activation strategy has been explored by coupling Al derived from spent AlH_3 with carbonyl Ni to construct an Al^*/Ni composite anode for electrochemical aluminum-hydride synthesis in a $LiAlH_4$/THF system. The optimized Al^*/Ni=7:3 anode delivers a high current density of 0.123 A cm^{-2}, which is 2.7 times that of pristine Al^*, and retains 80% of its initial current after 3 h of electrolysis, compared with 31% for the Al^* anode. The AlH_3 formation rate reaches 5.56 mmol h^{-1} with a Faradaic efficiency of 77.62%, representing a 2.84-fold increase in formation rate compared with the Al^* anode. The results of XPS analysis and DFT calculations are consistent with Ni-induced interfacial electronic redistribution and the formation of a polarized Al^*/Ni interfacial environment, which lowers the calculated AlH_4^- activation barrier and stabilizes the AlH_3^*+H^* final state, thereby promoting Al-H conversion and suppressing anode passivation. This work systematically introduces Ni-induced interfacial electronic modulation as an effective strategy for the electrochemical synthesis of aluminum-based hydrides using Al derived from spent AlH_3, providing a pathway toward a closed-loop aluminum-based hydride hydrogen-storage system.

KEYWORDS: aluminum hydride; interfacial engineering; electrochemical hydrogen storage; high current density; long-term stability.

1 Introduction

The development of high-density solid-state hydrogen-storage materials is critical for the safe and efficient storage, transportation, and distribution of hydrogen [1, 2]. Solid-state hydrogen-storage materials offer high safety, high volumetric density and potentially low cost under ambient conditions, making them attractive for large-scale and long-distance hydrogen logistics [3-5]. Among representative solid-state hydrogen-storage materials, MgH_2, $LiAlH_4$, $Mg(BH_4)_2$ and TiFe-based alloys have been extensively investigated. However, they generally suffer from high thermodynamic stability, elevated dehydrogenation temperatures, sluggish hydrogen sorption/desorption kinetics, or limited reversible hydrogen-storage capacity [6-9].

Aluminum-based hydrides are particularly promising hydrogen carriers because they combine high gravimetric hydrogen density with moderate working temperatures [10]. However, the direct reutilization of spent AlH_3 remains difficult because its regeneration back into aluminum hydride involves a high overall synthesis cost. Conventionally, the preparation of AlH_3 from Al metal requires either hydrogen pressures exceeding 2 GPa or organometallic synthesis processes involving substantial amounts of chemical reagents in solution [11, 12].

Organometallic and electrochemical synthesis methods have emerged as two promising routes for reducing the energy penalty associated with aluminum-hydride synthesis. Organometallic strategies mainly rely on Lewis-base ligands to stabilize AlH_3 intermediates thereby reducing the thermodynamic barrier for direct hydrogenation of aluminum. Lacina et al. [13] have demonstrated that tertiary amine ligands can trap and stabilize *in situ* generated AlH_3 under relatively mild conditions. In particular, trimethylamine reacts with Ti-activated Al and H_2 to form AlH_3-TMA at hydrogen pressures far below those required for direct Al/H_2 hydrogenation. Subsequently, TEDA-based

systems have further shown that Ti-doped or activated Al can reversibly form AlH_3-TEDA adducts with TEDA/H_2 under reduced hydrogen pressure [14, 15]. Structural studies by Ortmeyer et al. have revealed that the two nitrogen atoms of TEDA bridge adjacent AlH_3 units to generate one-dimensional $[AlH_3\text{-TEDA}]_n$ polymeric chains, thereby enhancing the stability of the alane adduct. Nevertheless, these approaches still rely on specific amine ligands, Ti-activated Al, pressurized H_2, or mechanochemical treatment leading to increased process complexity, separation costs and energy consumption. Therefore, developing an electrochemical synthesis strategy capable of directly regulating Al-H species conversion using spent-AlH_3-derived Al remains essential for the efficient reutilization of AlH_3. More importantly, this process could be coupled with renewable electricity, providing a potentially low-carbon route for synthesis and regeneration of aluminum-based hydride materials in principle.

Electrochemical synthesis could provide a milder alternative because the product distribution can be controlled through the applied potential and electrolyte composition. Zidan and co-workers at Savannah River National Laboratory proposed a cycle involving electrolysis and catalytic hydrogenation of spent aluminum to avoid high-pressure hydrogenation of aluminum and the formation of stable byproducts such as lithium chloride [16]. This work has demonstrated the feasibility of electrochemical AlH_3 synthesis using $MAlH_4$ (M=Li or Na) as the electrolyte, with TEDA-induced precipitation of AlH_3 used for indirect identification. The same team further proposed lithium chloride (LiCl) as an electrocatalytic additive in the cycle, which effectively improved the electrolysis efficiency and AlH_3 yield [17]. However, key parameters such as the electrolyte, potential window, and electrode materials have not been systematically investigated, while the properties and characteristics of the target products remain insufficiently defined.

Electrochemical synthesis of aluminum-based hydrides at high current density and with long-term stability imposes more stringent requirements on the interfacial stability and electronic transport of aluminum-based anodes. In electrochemical systems, coupling active materials with conductive phases is a well-established electrode-engineering strategy for improving electronic transport, facilitating interfacial charge transfer, and accelerating reaction kinetics [18-21]. Carbonyl Ni powder is a high-purity, micrometer-sized metallic material characterized by high electrical conductivity, good dispersibility, and a relatively uniform particle-size distribution. Unlike chemically inert carbonaceous additives, metallic Ni not only facilitates electron transport but also forms direct metal-metal interfaces with Al, thereby inducing interfacial electronic coupling and modulating the local electronic structure and reaction environment [22]. Related studies on Ni-based electrochemical materials have demonstrated that the tunable electronic structure and coordination environment of Ni can effectively regulate interfacial charge transfer, optimize the adsorption and activation of reaction intermediates, and consequently improve electrochemical reaction kinetics [23, 24]. Therefore, introducing carbonyl Ni powder into a highly active aluminum framework is expected to construct a conductive metallic network and Al^*/Ni heterointerfaces without compromising the intrinsic reactivity of Al powder, providing a feasible interfacial-regulation strategy to mitigate Al anode passivation in organic electrolytes, enhance interfacial electron transport, and stabilize continuous Al-H conversion.

Herein, an electrochemical strategy for the synthesis of aluminum-based hydrides using Al derived from spent AlH_3 has been demonstrated through Al^*/Ni heterointerface engineering. Highly active aluminum powder obtained from the dehydrogenation process of AlH_3, denoted as Al^*, has been coupled with carbonyl Ni powder to construct an Al^*/Ni composite anode, in which Al^* serves as a recyclable aluminum source and Ni functions as both a conductive framework and an interfacial electronic regulator. The intimate metal-metal contact between Al and Ni establishes continuous electron-transport pathways and is expected to induce interfacial charge redistribution and modulate the local electronic environment of Al sites near the Al^*/Ni contact region, thereby facilitating anodic Al-H conversion while suppressing passivation-induced current decay. Complementary DFT calculations have revealed that the promotional effect of the Al^*/Ni interface does not originate from simply strengthening the initial AlH_4^- adsorption. Instead, Ni incorporation modulates the local interfacial electronic structure and provides a more moderate AlH_4^- adsorption strength, which could lower the calculated activation barrier from 0.53 eV on Al^* to 0.39 eV on Al^*/Ni and stabilize the AlH_3^*+H^* final state from 0.38 to -0.23 eV. As a result, the optimized Al^*/Ni=7:3 anode delivers a steady-state current density of approximately 0.123 A cm^{-2} at 2.0 V vs. Ag/AgCl and an AlH_3 formation rate of 5.56 mmol h^{-1} with a Faradaic efficiency of 77.62%. The electrochemically generated product has been captured by TEDA and identified as an AlH_3-TEDA adduct by XRD, FTIR, DSC, and TPD/GC analyses. This work has established a chemically meaningful anode-interface design principle for electrochemical synthesis of lightweight hydride: regulating metal-metal interfacial electronic structure to reactivate spent aluminum and drive AlH_3 reformation under electrochemical conditions. By directly coupling dehydrogenated Al recycling with electrically-driven hydride synthesis, this strategy provides a new pathway toward green-electricity-driven aluminum-based hydride synthesis.

2 Materials and Methods

Materials

α-AlH_3 was purchased from Henan Nayu New Materials Co., Ltd. Carbonyl Ni powder (Hengbei Metal Materials Co., Ltd., particle size 2-7 μm) was used as the conductive modifying component. A 1.0 M lithium aluminum hydride solution in tetrahydrofuran ($LiAlH_4$/THF) was purchased from Macklin. 1,4-Diazabicyclo[2.2.2]octane (TEDA) and anhydrous tetrahydrofuran (THF) were purchased from Energy Chemical. All operations involving $LiAlH_4$ and AlH_3 were carried out in an Ar-filled glovebox, where the O_2 and H_2O contents were both below 0.1 ppm.

Just Accepted

Preparation of Al*/Ni Composite Anodes

Highly active aluminum powder (Al*) was obtained by temperature-programmed dehydrogenation of AlH_3. Specifically, AlH_3 was heated to 200 °C at a heating rate of 2 °C min^{-1} under Ar and held for 1.5 h to obtain dehydrogenated Al* powder. Al* and carbonyl Ni powders were weighed at the prescribed mass ratio and manually mixed using a mortar and pestle in an Ar-filled glovebox for 10 min. Carbonyl Ni powder was added to Al* in portions with alternating gentle grinding and mixing. Powder adhering to the mortar walls and pestle was periodically scraped off and reincorporated to promote uniform dispersion. Approximately 70 mg of the mixed powder was loaded into a 10.0 mm-diameter pellet die and pressed at 69.6-78.5 kN for 2 min using an NL-20S automatic tablet press, corresponding to a nominal pressure of 887-999 MPa. Different Al*/Ni mass ratios were denoted as 9:1, 8:2, 7:3, and 6:4.

Electrochemical Measurements

All electrochemical measurements were performed in an Ar-filled glovebox using a sealed three-electrode electrochemical cell (50 mL, Leton). A CHI650E electrochemical workstation (CH Instruments, Shanghai) was used. The pressed Al* or Al*/Ni pellet electrode served as the working electrode, a Pt plate (0.2 mm, 10 × 15 mm, Leton Electrochemistry) was used as the counter electrode, and a leak-free Ag/AgCl reference electrode (3.4 M KCl, Genode Technology Co., Ltd.) was used as the reference electrode. Unless otherwise stated, all potentials were recorded versus the leak-free Ag/AgCl reference electrode and were not converted to RHE or SHE. The electrolyte was a 1.0 M $LiAlH_4$/THF solution. Before testing, all electrode clamps and electrochemical cell components were cleaned, dried, and transferred into the glovebox. Cyclic voltammetry (CV) and linear sweep voltammetry (LSV) were performed without iR compensation, and the LSV scan rate was 50 mV s^{-1}. Potentiostatic electrolysis was conducted at a preset potential, with typical conditions of 2.0 V vs. Ag/AgCl for 3 h. During all measurements, the effective geometric area of each anode exposed to the electrolyte was maintained at one-half of the total area of the original electrode sheet.

The steady-state current density was calculated by averaging the current-density data recorded during the 2.5-3.0 h period of potentiostatic electrolysis. The current response was relatively stable within this time interval. The AlH_3 formation rate and Faradaic efficiency were determined from independent 1 h electrolysis experiments, whereas the 3 h chronoamperometric measurements were used to evaluate current stability and anode passivation behavior.

Non-Al Anode Control Experiment

To examine whether AlH_3 could be generated from the $LiAlH_4$/THF electrolyte in the absence of an Al-based anode, a control experiment was performed by replacing the Al*/Ni composite anode with a glassy carbon electrode. A three-electrode configuration was used, comprising a glassy carbon working electrode, a Pt plate counter electrode, and a leak-free Ag/AgCl reference electrode. The electrolyte concentration and volume, applied potential, electrolysis duration, and subsequent TEDA-trapping procedure were identical to those used in the Al*/Ni experiment. After electrolysis, TEDA was added to capture any potentially generated AlH_3. Only slight turbidity was observed, and insufficient solid could be recovered by centrifugation for further characterization, indicating a very limited amount of recoverable solid under these conditions. Therefore, the GC control cannot quantitatively resolve the contributions of competing reactions on the Al-based anodes, and the reported Faradaic efficiency should be interpreted in the context of the explicitly stated stoichiometric assumption for the Al-involving reaction.

Trapping and Verification of the AlH_3-TEDA Adduct

After potentiostatic electrolysis, 20 mL of the electrolyte was collected and filtered through a membrane to remove solid particles or detached electrode fragments. TEDA was then added to the filtrate to capture solvated AlH_3 or Al-H intermediates generated during electrolysis. After TEDA addition, a white precipitate gradually formed in the solution. The precipitate was collected by centrifugation at 8500 rpm for 2 min. The obtained solid was washed three times with anhydrous THF to remove residual $LiAlH_4$, TEDA, and soluble byproducts, and then dried under an Ar atmosphere. The resulting white solid was denoted as AlH_3-TEDA and used for subsequent structural and thermal analyses.

Materials and Product Characterization

Scanning electron microscopy (SEM, Regulus 8230) was used to observe the surface morphology of the electrode materials before and after electrolysis, and energy-dispersive X-ray spectroscopy (EDS) was used to analyze the elemental distribution. Transmission electron microscopy (TEM, JEOL JEM-2100F) was used to observe the microscopic morphology of Al* or the composite materials. Brunauer-Emmett-Teller (BET, Micromeritics ASAP 2460) analysis was used to determine the specific surface area and pore-structure characteristics of the electrode materials. X-ray diffraction (XRD, Bruker D8 Advance) was used to analyze the phase composition of the electrode materials, electrode products after electrolysis, and AlH_3-TEDA adducts. FTIR spectroscopy was performed using a Thermo Scientific Nicolet iS50 FTIR spectrometer operated at room temperature. Differential scanning calorimetry (DSC) was used to evaluate the thermal decomposition behavior and thermal stability of the AlH_3-TEDA adduct. X-ray photoelectron spectroscopy (XPS, Axis Ultra DLD Kratos) was used to analyze the elemental composition and chemical states of the anode surface before and after electrolysis. Temperature-programmed desorption (TPD) coupled with gas chromatography (GC, jieDao GC1690, Ar as the carrier gas) was used to analyze the hydrogen-release behavior of the AlH_3-TEDA adduct and assist in calculating the coordination ratio between AlH_3 and TEDA.

Determination of the AlH_3 formation rate and Faradaic efficiency

The amount of AlH_3 was estimated from the AlH_3-TEDA product captured by TEDA after electrolysis. The coordination number and quantitative composition of the AlH_3-TEDA adduct were determined by combining temperature-programmed desorption (TPD) with gas chromatography (GC, jieDao GC1690, Ar as the carrier gas) to establish the molecular formula. The AlH_3 formation rate

Just Accepted

was defined as the amount of AlH_3 generated per unit electrolysis time:

$$r_{AlH_3}=\frac{n_{AlH_3}}{t}$$

where $nAlH_3$ is the actual amount of AlH_3 and t is the electrolysis time. Because the electrolyte volume, electrode area, and electrolysis time were kept constant in different experiments, the formation rate was reported in mmol h^{-1}.

The AlH_3-TEDA adduct was heated in the TPD experiment to collect the gas released during dehydrogenation (a mixture of H_2 and Ar), from which the total gas capacity of the sample was calculated. The H_2 purity in the mixed gas was determined from the gas-chromatography peak area, allowing the amount of hydrogen produced to be calculated and the coordination number and structural formula of AlH_3 and TEDA to be inferred.

On the basis of the above calculation, potentiostatic electrolysis was performed for 1 h in the three-electrode system, followed by addition of excess TEDA. The product was washed three times with equal volumes of anhydrous THF, centrifuged and dried under an Ar atmosphere, and then weighed to calculate the Faradaic efficiency. The experiment was repeated.

$$FE=\frac{m\times n\times F}{Q_{total}}$$

F is the Faraday constant (96485 C mol^{-1}), n is the actual amount of the target product (mol), $Q_{total}=\int I(t)dt$ is the total charge passed (C), and m is the number of electrons corresponding to the generation of 1 mol AlH_3. For the Al^*-participating anodic oxidation pathway, the number of electrons corresponding to the generation of 1 mol AlH_3 is: m=3/4= 0.75.

DFT Calculations: We used the DFT as implemented in the Vienna Ab initio simulation package (VASP) in all calculations[31, 32]. The exchange-correlation potential is described by using the generalized gradient approximation of Perdew-Burke-Ernzerhof (GGA-PBE) [33]. The projector augmented-wave (PAW) method is employed to treat interactions between ion cores and valence electrons[34, 35]. The plane-wave cutoff energy was fixed to 450 eV. Gamma point was used for structural optimization. Given structural models were relaxed until the Hellmann-Feynman forces smaller than 0.03 eV/Å and the change in energy smaller than $1E^{-5}$ eV was attained. The Gibbs free-energy changes were calculated as $\Delta G=\Delta E+\Delta EZPE-T\Delta S$, where ΔE is the DFT electronic energy difference, ΔEZPE is the zero-point energy correction, and ΔS is the entropy change at 298.15 K.

Notation

Throughout this work, Al^* denotes the highly active aluminum powder obtained by the dehydrogenation of α-AlH_3, and Al^*/Ni denotes the composite anode composed of Al^* and carbonyl Ni powder. The superscript asterisk in Al^* is used solely as part of the sample designation. In expressions such as AlH_3^* and H^*, the asterisk denotes a surface-bound species according to conventional surface-science notation. Unless otherwise specified, all Al^*/Ni ratios refer to mass ratios.

3 Results and Discussion

3.1 Electrochemical Synthesis of Aluminum-Based Hydrides

AlH_3 is a high-density solid-state hydrogen-storage material whose advantages arise not only from its theoretical hydrogen capacity exceeding 10 wt.% (Figure S1, Supporting Information), but also from its ability to release hydrogen rapidly under mild conditions [10]. Figure 1a summarizes the advantages and challenges of AlH_3 at the materials level: high hydrogen capacity, favorable dehydrogenation kinetics, and mild hydrogen-release behavior collectively endow AlH_3 with value as a solid-state hydrogen carrier, while electrochemical in situ synthesis could provide a new route to overcome the poor reversibility after dehydrogenation and the high cost associated with conventional synthesis.

Figure 1b illustrates the mechanism of the closed-loop dehydrogenation-regeneration cycle underlying this work. After hydrogen release, AlH_3 is converted into metallic Al, which can participate in the electrochemical reformation of AlH_3 through the interfacial activation of AlH_4^- on the Al^*/Ni composite anode. The electronically modulated Al^*/Ni interfacial environment facilitates the conversion of adsorbed AlH_4^- species into AlH_3 intermediates, providing a pathway toward closing the AlH_3/Al cycle.

Figure 1c further extends this materials cycle to the energy-system level by constructing a renewable-electricity-driven closed-loop AlH_3 fuel chain. In this system, renewable electricity powers an electrochemical regeneration unit that converts dehydrogenated Al back into AlH_3. The recycled AlH_3 serves as a high-density hydrogen carrier, enabling hydrogen release under mild conditions for commercial, transportation, and industrial applications. Furthermore, the Al species after hydrogen release can be returned to the electrochemical synthesis unit, providing a conceptual pathway toward closing the cycle. Thus, green electricity derived from solar or wind energy could be converted and stored in a transportable and dispatchable hydrogen carrier based on utilization and recycle of AlH_3 providing a new route for converting sustainable electricity into end-use hydrogen carrier.

Uncorrected

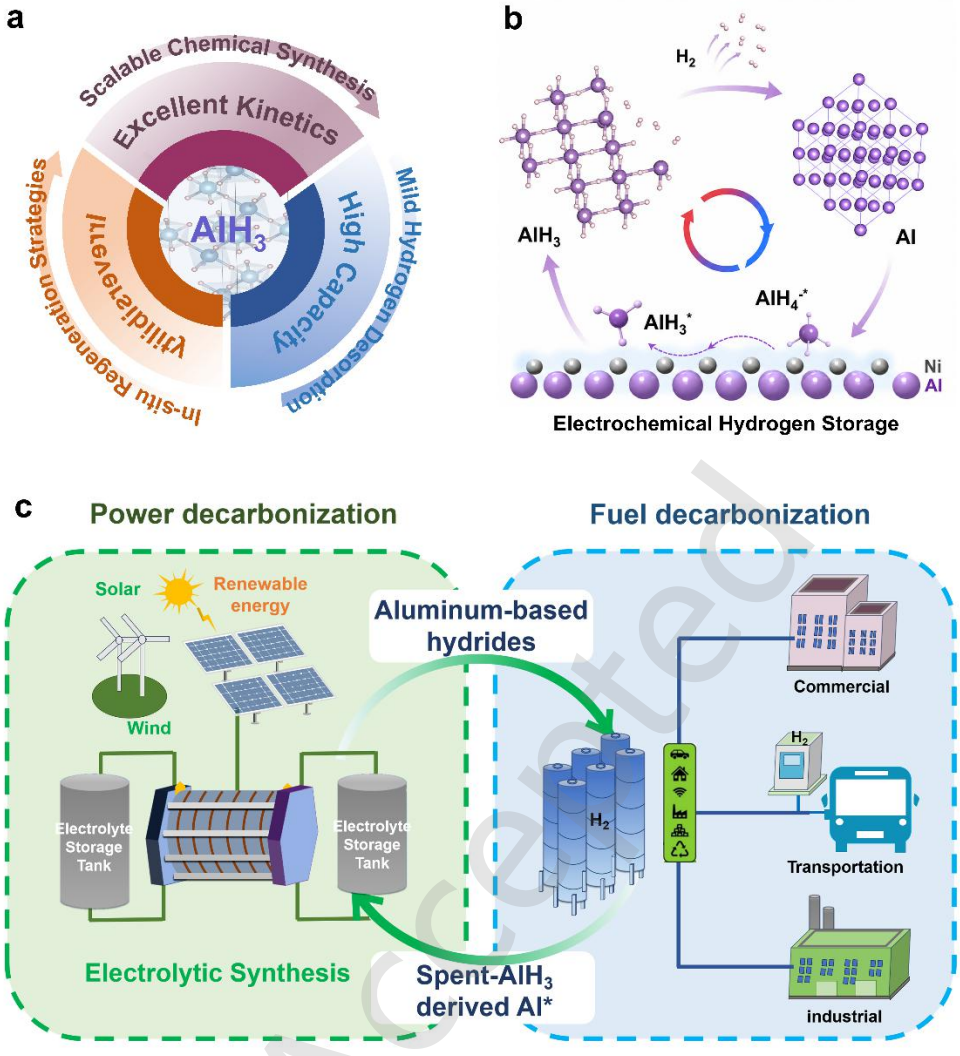


Figure 1. Conceptual framework for the electrochemical regeneration and closed-loop utilization of AlH_3. (a) Schematic illustration of the advantages and regeneration challenges of AlH_3. (b) Schematic illustration of the reversible dehydrogenation-electrochemical regeneration cycle between AlH_3 and Al, involving the interfacial activation of AlH_4^- and formation of AlH_3 intermediates on the Al^*/Ni composite anode. (c) Renewable-electricity-driven electrochemical synthesis strategy.

3.2 Synthesis and Structural Characterization of Al^*/Ni Composite Anodes

The synthesis procedure of the Al^*/Ni anode material has been illustrated in Figure 2a. The pristine α-AlH_3 was subjected to temperature-programmed heating to 200 °C and maintained at this temperature for 1.5 h to obtain the byproduct of aluminum (Al^*) after dehydrogenation, which was then homogeneously mixed with carbonyl Ni powder and pressed into pellets to form the anode. Powder X-ray diffraction (XRD, Figure S2a, Supporting Information) and scanning electron microscopy (SEM, Figures S2b and S2c, Supporting Information) have indicated that the pristine α-AlH_3 possesses high phase purity and a well-defined cubic morphology. TPD (Figure S3a, Supporting Information) shows a hydrogen release of 9.923 wt.%, close to the theoretical hydrogen content of AlH_3 (approximately 10.1 wt.%), with a plateau before 200 °C, supporting essentially complete dehydrogenation. XRD (Figure S3b, Supporting Information) and transmission electron microscopy (TEM, Figure S3d, Supporting Information) have confirmed that the obtained pure byproduct aluminum consists predominantly of the Al phase, with a measured lattice spacing of 0.205 nm corresponding to the Al (200) plane, indicating a well-crystallized face-centered cubic Al phase. SEM images (Figure S3c, Supporting Information) reveal that numerous micrometer-scale pores and channels are generated during the decomposition of α-AlH_3, while the spatial connectivity of metallic Al has been retained *in situ*. As shown in Figure 2b, no obvious impurity phases or newly formed crystalline phases have been observed in the Al^*/Ni electrode material.

The HRTEM image in Figure 2c shows lattice spacings of 0.196 and 0.228 nm, which correspond to the Al (200) and (111) planes, respectively, whereas another distinct lattice fringe with a spacing of 0.208 nm is assigned to the Ni (111) plane. Figure 2d presents the SEM morphology of the Al^*/Ni composite, in which the carbonyl Ni particles are distributed within the micrometer-scale pores and channels of Al^*, providing spatial contact between the two metallic components and favoring the formation of a conductive network. Combined with the energy-dispersive X-ray spectroscopy (EDS) elemental maps in Figure 2e, the results could confirm a relatively homogeneous spatial distribution

Just Accepted

of Al and Ni throughout the optimized Al*/Ni=7:3 composite without obvious large-scale Ni aggregation.

Notably, EDS analysis of the Al*/Ni series after electrolysis (Figure S4, Supporting Information) shows discernible Ni aggregation when the Ni fraction is increased to Al*/Ni=6:4. BET analysis reveals an additional control for distinguishing interfacial effects from a simple surface-area contribution. As shown in Figure 2f, Figure S5, and Table S1 (Supporting Information), the BET specific surface areas of the post-electrolysis Al*/Ni=7:3 and Al anodes are 6.04 and 26.74 m^2 g^{-1}, respectively. Therefore, the enhanced electrochemical performance cannot be attributed to an increase in physical surface area, supporting the importance of Ni-induced structural and interfacial effects.

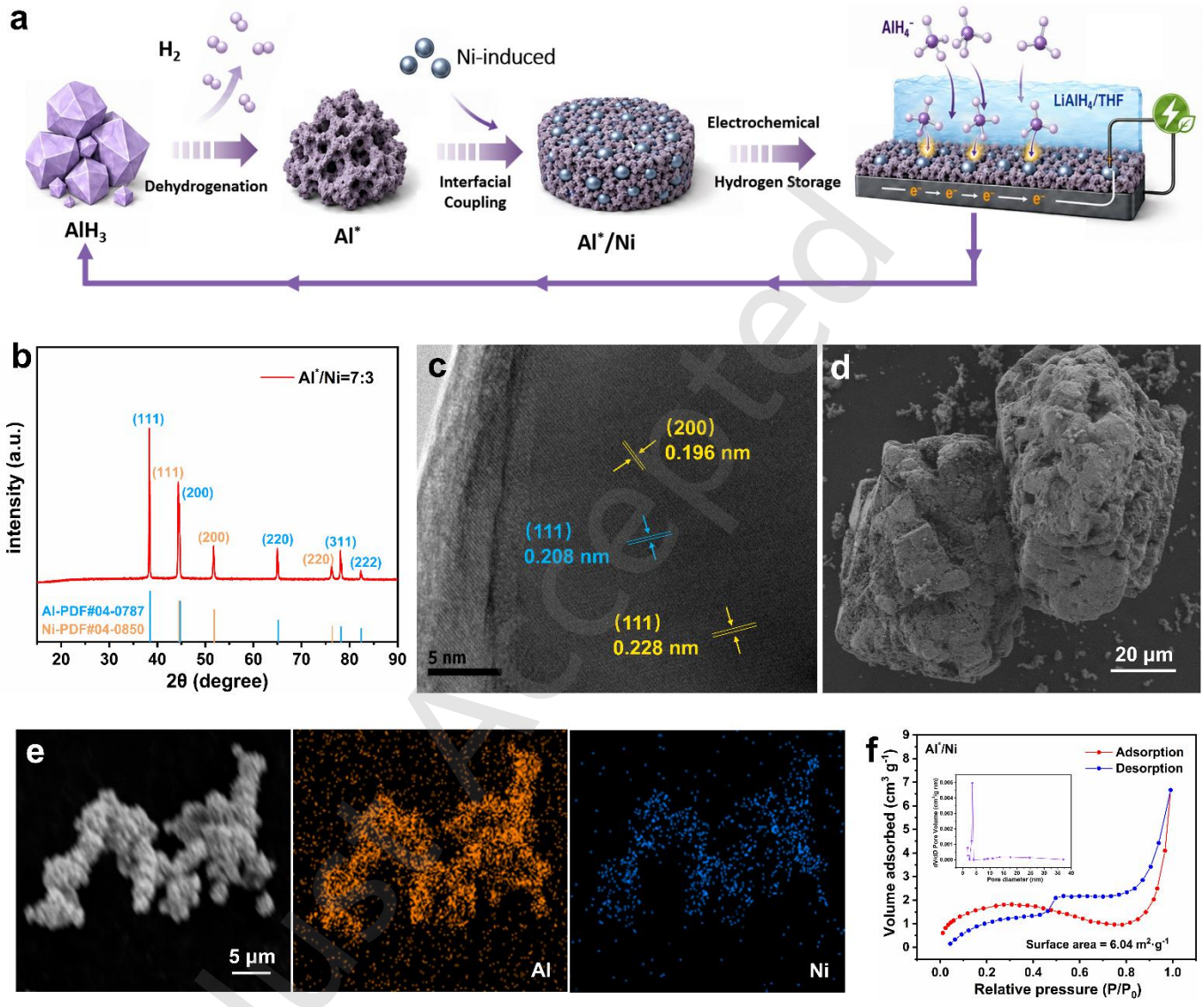


Figure 2. Synthesis and structural characterization of the Al*/Ni composite anode. (a) Schematic illustration of the preparation of the Al*/Ni composite anode. (b) XRD pattern of the as-prepared Al*/Ni (7:3). (c) TEM image of Al*/Ni (7:3). (d) HRSEM image of the as-prepared Al*/Ni (7:3). (e) Representative SEM image and corresponding Al and Ni elemental maps of the as-prepared Al*/Ni (7:3). (f) BET analysis of the Al*/Ni (7:3) anode material after electrolysis.

3.3 Electrochemical Performance and Hydride Formation

To precisely control and analyze the electrochemical process, all reactions were conducted in a three-electrode configuration. Firstly, AlH_3 was subjected to temperature-programmed dehydrogenation to obtain dehydrogenation-derived Al* powder, which was subsequently used as the active Al source in the three-electrode electrochemical system.

As shown in Figure 3a, the Al* anode exhibits a distinct oxidation response at -2.33 V vs. Ag/AgCl, indicating that Al*/AlH_4^--related species could undergo electrochemical oxidative conversion at a relatively low anodic potential, thereby providing a possible electrochemical window for subsequent AlH_3 formation. In contrast, Al*/Ni exhibits a less pronounced peak-like feature in a similar potential region but a higher anodic current at more positive potentials, indicating that Ni incorporation modifies the voltammetric response and enhances the overall anodic current response. The polarization behaviors of Al* and Al*/Ni anodes with different Al*/Ni ratios are further compared by LSV (Figure 3b). At the same applied potential, the Al*/Ni anodes exhibit

Just Accepted

higher current densities than Al*. With increasing Ni content, the current response initially increases, reaches a maximum at Al*/Ni=7:3, and then decreases upon further increasing the Ni content. Among them, Al*/Ni=7:3 delivers the highest current output, suggesting that the introduction of an appropriate amount of Ni could effectively improve electron transport within the electrode and promote the anodic interfacial oxidation process. However, further increasing the Ni content does not necessarily lead to better overall performance, as excessive Ni might dilute the Al active sites and alter the relative contributions of the target reaction and competing reactions.

In addition, to further evaluate the stability of the composite anodes, potentiostatic electrolysis tests have been performed at 2 V vs. Ag/AgCl for 3 h using Al*/Ni anodes with different compositions (Figure 3c). Compared with the commercial Al anode, the Al* anode exhibited a more rapid current decay during the 45 min potentiostatic electrolysis test (Figure S6, Supporting Information). The pronounced passivation-induced current decay observed at the initial stage of electrolysis, together with the rapid decrease and subsequent low-level stabilization of the current density, has indicated that a passivation layer readily forms on the electrode surface and hinders the sustained reaction. In contrast, the Al*/Ni composite anodes have exhibited overall higher and more stable current densities, among which Al*/Ni=7:3 maintains a high current output throughout the electrolysis process, demonstrating superior interfacial reaction activity and resistance to passivation.

The normalized current curves further confirm this behavior (Figure 3d): after 3 h, the Al* electrode retains only 31% of its initial current, whereas the Al*/Ni=7:3 electrode maintains 80% of its initial current, clearly outperforming the 8:2 and 6:4 electrodes. This result indicates that an appropriate amount of Ni can significantly alleviate electrode passivation and sustain the anodic reaction.

Figure 3e has compared the steady-state current densities quantitatively at different Ni contents. The steady-state current density of the Al* electrode is only 0.045 A cm^{-2}, whereas it increases markedly with increasing Ni content and reaches a maximum value of 0.123 A cm^{-2} at a Ni content of 30 wt.%, which is 2.7-fold that of Al*. When the Ni content is further increased to 40 wt.%, the steady-state current density decreases to 0.088 A cm^{-2}, suggesting that excessive Ni reduces the proportion of effective Al reaction sites or alters the interfacial reaction balance. Therefore, Al*/Ni=7:3 could be identified as the optimal anode composition, combining high current density with excellent stability. Based on this optimal composition, the effect of the applied potential on the electrolysis process has been further investigated (Figure 3f). As the potential increases from 1.0 V to 2.0-2.5 V vs. Ag/AgCl, the current density increases significantly with relatively moderate decay, indicating that a higher anodic driving force is favorable for promoting the oxidative conversion of AlH_4^-/Al*-related species. At 3.0 V vs. Ag/AgCl, although the initial current density is the highest, a more pronounced current decay is observed suggesting that an excessively positive anodic potential might intensify parasitic reactions and accelerate interfacial deactivation, thereby decreasing the stability and selectivity of the electrolysis process.

To examine the surface morphological changes associated with the observed current-decay behavior, SEM characterization was performed on the post-electrolysis electrodes (Figure S7, Supporting Information). The images show the formation of a dense surface layer on Al*, which limits the continued exposure of active Al sites and is consistent with the pronounced current decay observed during electrolysis. In contrast, the Al*/Ni electrode retains an open and interconnected surface without a continuous dense covering layer, even after electrolysis at an anodic potential as high as 3 V vs. Ag/AgCl. This morphology demonstrates that Ni incorporation could effectively mitigate surface-layer accumulation and preserve accessible reaction sites, contributing to improved current stability.

To quantitatively evaluate the promoting effect of the Al*/Ni composite anode on the electrochemical recycling of AlH_3, the AlH_3 formation rate and Faradaic efficiency have been determined in an independent 1 h electrolysis experiment and compared with those obtained using the Al* anode under otherwise identical conditions. As shown in Figure 3g, the Al*/Ni anode achieves an AlH_3 formation rate of 5.56 mmol h^{-1}, revealing 2.84-fold that obtained with the Al* anode. Meanwhile, its Faradaic efficiency is 1.37-fold that of the Al* anode, indicating that the introduction of Ni not only significantly enhances the formation rate of AlH_3 but also improves charge utilization efficiency. These results demonstrate that the Al*/Ni interface is beneficial for enhancing anodic electron transport and interfacial reaction activity, while also mitigating the current decay caused by passivation of the pure Al surface to some extent. Subsequently, as shown in Figure 3h, when the potential is increased from -1.5 to 2 V vs. Ag/AgCl, the AlH_3 formation rate increases markedly from 0.80 to 5.56 mmol h^{-1}, corresponding to an approximately 7-fold enhancement, while the Faradaic efficiency remains essentially unchanged. This result reveals that 2 V vs. Ag/AgCl could substantially increase the product formation rate without an obvious sacrifice in selectivity. Further potential-dependent results have been shown in Figure 3i indicating that the AlH_3 formation rate gradually raises with the increasement of the potential from 1 to 2 V vs. Ag/AgCl. When the potential is further increased to 2.5 V vs. Ag/AgCl, the Faradaic efficiency decreases markedly and the formation rate declines simultaneously. Therefore, 2 V vs. Ag/AgCl should achieve a favorable balance among AlH_3 formation rate, Faradaic efficiency and side-reaction suppression as shown in Fig. 3.

Not Accepted

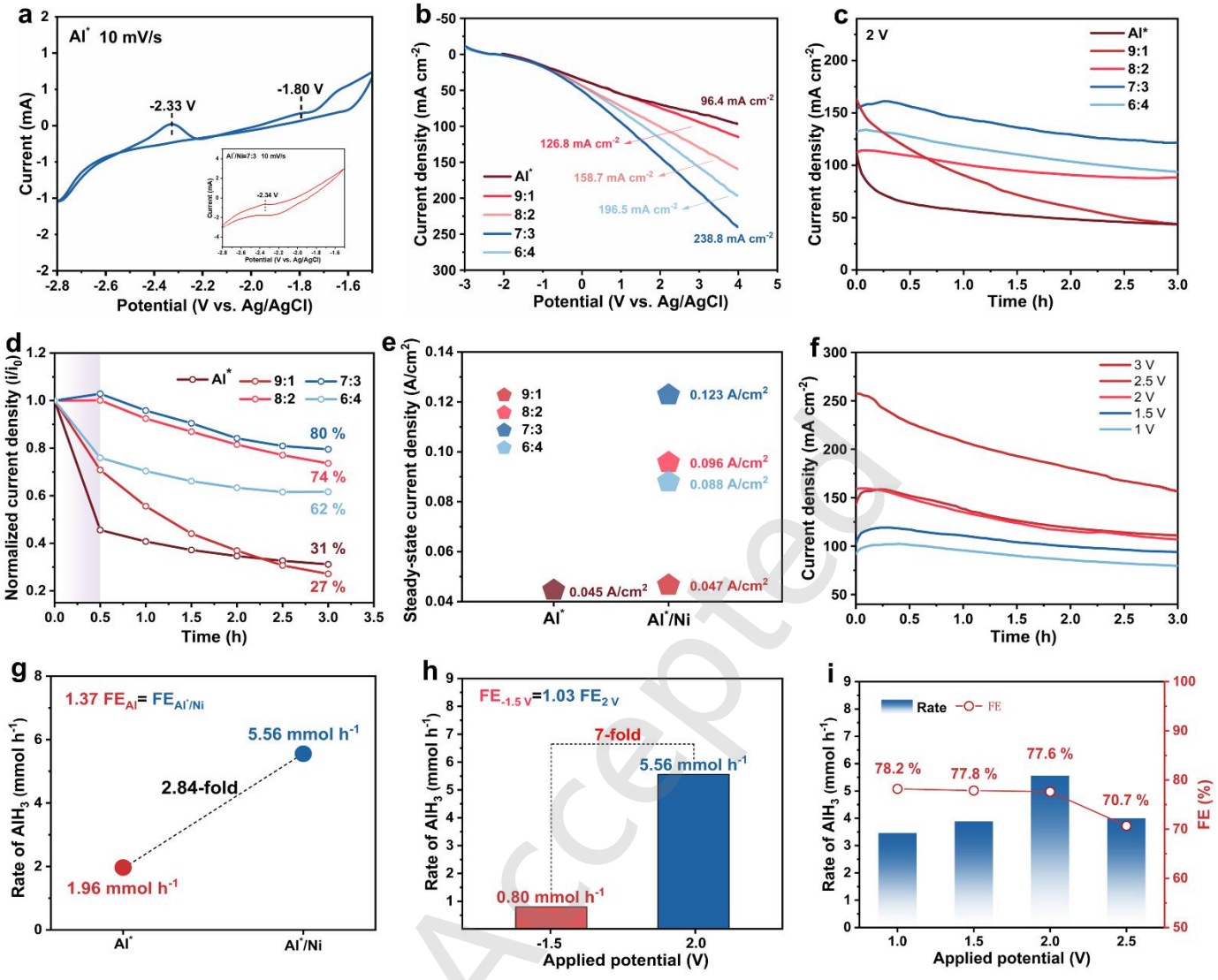


Figure 3. Electrochemical characterization. (a) Cyclic voltammograms recorded using Al* and Al*/Ni as the anodes. (b) LSV curves of Al*/Ni anodes with different Ni contents. (c) j-t curves of Al*/Ni anodes with different Ni contents. (d) Normalized current (i/i_0)-time curves of Al*/Ni anodes with different Ni contents at 2 V vs. Ag/AgCl. (e) Steady-state current densities of Al*/Ni anodes with different Ni contents after electrolysis at 2 V vs. Ag/AgCl for 3 h. (f) j-t curves recorded at different applied potentials. (g) AlH_3 formation rate obtained using Al* and Al*/Ni as anode materials at 2 V vs. Ag/AgCl. (h) AlH_3 formation rate obtained using Al*/Ni as the anode material at -1.5 and 2 V vs. Ag/AgCl. (i) AlH_3 formation rate and Faradaic efficiency at different applied potentials.

Figure S8a (Supporting Information) schematically illustrates the synthetic pathway of the AlH_3-TEDA adduct: the AlH_3 generated in the three-electrode system dissolves in tetrahydrofuran to form a coordinated intermediate (Figure 4a), followed by the addition of triethylenediamine (TEDA), which induces the precipitation of AlH_3 in the form of a more stable white solid, namely the AlH_3-TEDA adduct, thereby indirectly confirming the formation of AlH_3 [17, 25]. To systematically evaluate the electrolysis products obtained using Al*/Ni anode materials with different compositions, potentiostatic electrolysis has been conducted at 2 V vs. Ag/AgCl for 3 h after which the resulting AlH_3-TEDA adducts were characterized by X-ray diffraction (Figure S8b, Supporting Information) and Fourier-transform infrared spectroscopy (Figure S8c, Supporting Information). The results have shown that the obtained diffraction patterns would be in good agreement with the reported standard pattern of phase-pure AlH_3-TEDA with no additional diffraction peaks from impurity phases, confirming the successful synthesis of the target adduct within this compositional range [25]. FTIR analysis further reveals the molecular structural features of the product, in which a pronounced absorption band at 1701 cm^{-1} is assigned to the stretching vibration of the Al-H bond [17, 26]. Differential scanning calorimetry (DSC) has been carried out and analyzed in Figure 4c to certify the thermal stability of the AlH_3-TEDA adducts obtained at 2 V vs. Ag/AgCl for 3 h and performed at a linear heating rate of 10 °C min^{-1}. The DSC curves clearly exhibit an intense endothermic peak of all samples in the temperature range from 230 to 236 °C, corresponding to the main decomposition process of AlH_3-TEDA adducts [27]. With increasing incorporation of carbonyl nickel in the anode, namely with an increasing Ni fraction, the peak temperature of the main decomposition event shifts to higher temperatures systematically, increasing from 231.7 °C for Al*/Ni=9:1 to a maximum of

Just Accepted

235.1 °C for Al*/Ni=6:4. The thermograms display a single sharp main decomposition peak indicating that increasing the Ni content affects the thermal stability of the isolated AlH_3-TEDA adducts related to the Ni-induced modification of the AlH_3 formation environment and the reduced proportion of thermally unstable Al-H species. When commercial aluminum powder was used as the electrode material, XRD (Figure S9a, Supporting Information), FTIR (Figure S9b, Supporting Information), and DSC (Figure S9c, Supporting Information) revealed less well-defined structural features of the recovered product, while quantitative analysis (Figure S9d, Supporting Information) confirmed a substantially lower amount of AlH_3-TEDA under the same electrolysis conditions.

Figures 4d-f systematically investigate the XRD, FTIR, and DSC profiles of the products obtained after potentiostatic electrolysis for 3 h at different applied potentials of 1, 1.5, 2, 2.5, and 3 V vs. Ag/AgCl using the optimized Al*/Ni=7:3 anode. The XRD phase analysis (Figure 4d) shows that the diffraction patterns are in good agreement with the standard pattern of the AlH_3-TEDA adduct at 1, 1.5, and 2 V vs. Ag/AgCl. When the potential is increased to 2.5 and 3 V vs. Ag/AgCl, weak but distinguishable impurity peaks appear at approximately 20° representing that excessively high potentials might lead to the local formation of trace crystalline byproducts. The FTIR spectra in Figure 4e further show that all samples exhibiting a pronounced absorption band at approximately 1701 cm^{-1}, which is assigned to the asymmetric stretching vibration of the Al-H bond. The similar peak position and spectral profile observed over the investigated potential range indicate that the products possess comparable local Al-H bonding environments and that no pronounced change in the AlH_3-TEDA coordination structure is detectable by FTIR. DSC thermal analysis (Figure 4f) shows that the main decomposition peaks have been concentrated within a narrow temperature range of 230-235 °C, indicating that the overall thermal stability of AlH_3-TEDA adducts remains largely consistent within the examined potential range. The sharp main decomposition peaks suggest good homogeneity in the thermal behavior of the major product. Although higher potentials increase the current density, competitive decomposition of aluminum hydride species also has been enhanced, thereby leading to a decrease related to Faradaic efficiency. Therefore, the potential range of ≤2.0 V vs. Ag/AgCl has been regarded as more favorable for balancing the formation rate of products, entirely Faradaic efficiency and suppression of side reactions while maintaining the stable bulk thermal behavior of AlH_3-TEDA.

To determine the apparent composition of the adduct and enable quantitative analysis of the product, temperature-programmed desorption (TPD) combined with gas chromatography (GC) has been employed to characterize the AlH_3-TEDA adduct. Figure 4g shows the TPD profiles obtained from three independent measurements. Gas evolution had begun at 200 °C and been essentially stopped at around 245 °C. After cooling the TPD effluent, white crystals had been collected from the condensed fraction. Their XRD pattern (Figure 4h) was largely consistent with that of crystalline TEDA, indicating that at least a substantial fraction of TEDA volatilized during heating and recrystallized upon cooling, with no detectable crystalline decomposition products. The remaining non-condensable gas consisted of H_2 and the Ar carrier gas. A 1.0 mL aliquot of the non-condensable gas mixture was withdrawn using a gas-tight syringe and analyzed by GC. Meanwhile, 1.0 mL of pure H_2 was analyzed as an external standard under identical chromatographic conditions. Based on the GC results (Table S2, Supporting Information), the volume fraction of H_2 in the H_2/Ar gas mixture was estimated. The amount of H_2 released from the sample was subsequently calculated by combining the GC-determined H_2 volume fraction with the total amount of gas released during the TPD measurement. Three repeated parallel experiments gave an average coordination number of 1.4. As illustrated by the adduct formation process and the three-dimensional monomeric structural formula (Figure 4b), the adduct forms Al-N polymeric chains, with the structural unit corresponding to a 1:1 coordination polymer chain. However, the quantitative composition of overall samples gives an apparent TEDA-to-AlH_3 ratio of 1.4 due to terminal TEDA or free/weakly bound TEDA. This extended network, together with the chemically saturated environment provided by terminal TEDA, accounts for the stability of the adduct.

Just Accepted

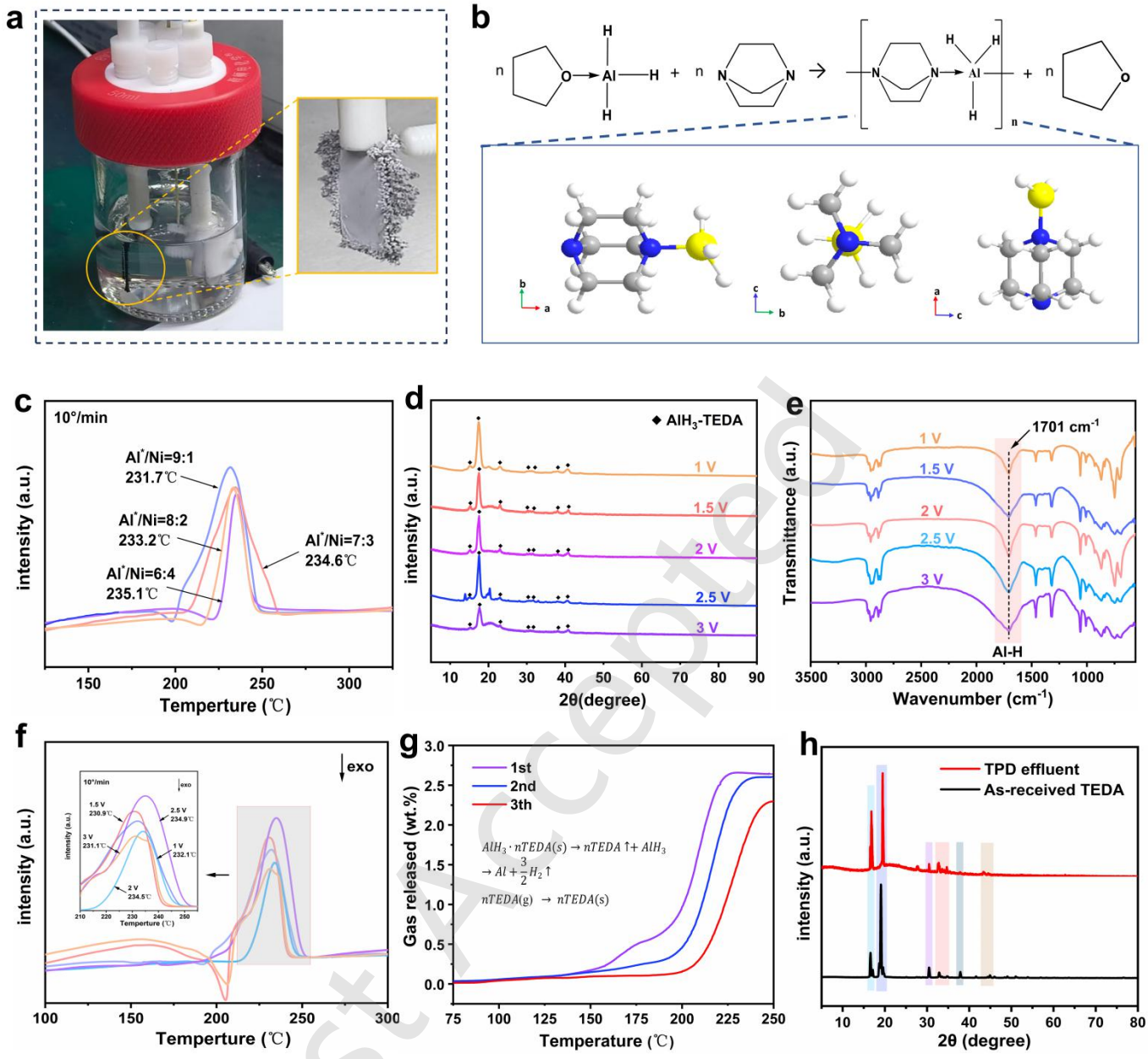


Figure 4. Structural, thermal, and compositional characterization of the products. (a) Photograph of the three-electrode cell and enlarged view of the cathodic deposit after potentiostatic electrolysis using Al*/Ni=7:3 as the anode. (b) Schematic illustration of TEDA-assisted displacement of coordinated THF from electrochemically generated AlH_3–THF, together with ball-and-stick representations of the resulting AlH_3–TEDA adduct viewed along different crystallographic directions. Al, N, C, and H atoms are shown in yellow, blue, gray, and white, respectively.(c) DSC profiles of AlH_3-TEDA obtained using Al*/Ni anodes with different ratios. (d) XRD patterns of AlH_3-TEDA obtained at different applied potentials. (e) FTIR spectra of AlH_3-TEDA obtained at different applied potentials. (f) DSC profiles of AlH_3-TEDA obtained at different applied potentials. (g) TPD profiles of AlH_3-TEDA. (h) XRD pattern of the condensed product.

Just Accepted

3.4 Electrochemical Reaction Process

Subsequently, the post-electrolysis electrodes and attached products were systematically characterized to further reveal the interfacial evolution, product distribution, and possible reaction pathways during the electrochemical formation of AlH_3. Figures 5a and 5b schematically illustrate the electrolysis behaviors when Al* and Al*/Ni=7:3 are used as the anodes, respectively. During electrolysis, the Al* anode readily undergoes interfacial reactions with the electrolyte, forming a covering passivation layer that hinders the continuous exposure of active Al sites as well as electron/ion transport, thereby leading to current decay. In contrast, in the Al*/Ni composite anode, Ni and Al* construct a metal-metal heterointerface that can induce interfacial charge redistribution, rendering adjacent Al species relatively electron-deficient and thus more prone to oxidative conversion under the anodic potential. Meanwhile, Ni, serving as a conductive framework, could enhance electron transport within the electrode and mitigate the formation of a continuous dense passivation film, thereby delivering higher current density and long-term electrochemical activity.

Simultaneously, to further elucidate the mechanistic role of carbonyl nickel powder in the electrochemical synthesis of aluminum hydride, the surface chemical states of the anode materials before and after electrolysis were analyzed by high-resolution X-ray photoelectron spectroscopy (XPS). The Al 2p spectra in Figures 5d and 5e have shown that both Al^* and Al^*/Ni samples before electrolysis contain metallic Al and Al^{3+} species with the Al^{3+} signal mainly originating from the native oxide layer on the Al^* surface and unavoidable surface oxidation during sample transfer [28, 29]. After electrolysis, the Al 2p peak of the Al^*/Ni sample exhibits a positive shift of approximately 0.3 eV relative to that of the pristine Al^*/Ni sample, indicating that the Al species are located in a more electron-deficient chemical environment. Meanwhile, in the Ni 2p spectrum shown in Figure 5f, the main Ni peak shifts toward lower binding energy by approximately 0.3 eV after electrolysis, indicating an increased electron density around Ni. The opposite shifts of the Al 2p and Ni 2p signals are consistent with interfacial electronic redistribution between Al- and Ni-rich regions. Together with the charge-density-difference calculations, these observations support the formation of an electronically polarized Al^*/Ni interfacial environment. Further comparison of the Al 2p spectra of Al^*/Ni electrodes with different compositions (Figure S10a-c, Supporting Information) reveals that the Al^*/Ni=7:3 sample exhibits the largest positive binding-energy shift, indicating the most pronounced interfacial charge redistribution. In contrast, when the Ni content is further increased to Al^*/Ni=6:4, the Al 2p shift decreases, indicating that excessive Ni may shield active Al sites and reduce the effective Al^*/Ni reactive interface. These results clarify that an appropriate amount of Ni not only improves the continuity of electronic transport within the electrode but also induces the formation of an activated Al^*/Ni interface during electrolysis, thereby optimizing the anodic reaction kinetics.

To clarify the phase composition of products formed in different regions after electrolysis, potentiostatic electrolysis was performed using a fixed Al^*/Ni=7:3 anode, and the products in the cathodic region were separated and collected. These products were analyzed in combination with photographs of the corresponding XRD results (Figure S11, Supporting Information). Subsequently, the surface of the anode material, the white film attached to the cathode, and the black substance on the cathode surface were separately characterized by XRD (Figures 5g-i). Comparison with standard PDF cards shows that no new phase is formed on the surface of the anode material after electrolysis, indicating that the Al^*/Ni framework maintains relative stability during the reaction, while a small number of AlH_3-related species is attached to the electrode surface. The black substance near the cathode is mainly assigned to metallic Al, whereas the white film mainly corresponds to Li_3AlH_6 and LiH. The formation of these cathode-side species suggests that $LiAlH_4$ or Al-containing intermediates undergo side reactions at the cathode[17, 30]. Notably, to assess the contribution of electrolyte-related reactions at 2.0 V vs. Ag/AgCl and further examine the role of the Al-based anode in AlH_3 formation, control experiments were performed using a glassy carbon (GC) electrode in place of the Al^*/Ni anode. LSV and potentiostatic measurements in the actual $LiAlH_4$/THF electrolyte revealed a relatively low but measurable anodic background current at this potential, indicating that electrolyte-related reactions cannot be excluded. Under identical electrolyte conditions, applied potential, and electrolysis duration, only slight turbidity was observed upon adding TEDA after electrolysis, suggesting that direct electrochemical oxidation of the $LiAlH_4$/THF electrolyte does not readily yield recoverable AlH_3-TEDA in the absence of an Al^* anode (Figure S12, Supporting Information). These observations highlight the importance of the Al-based anode in obtaining recoverable AlH_3-TEDA under the investigated conditions and are consistent with the proposed Al^*-involving reaction pathway. Based on the above results, Figure 5c proposes the mechanism for the electrochemical formation of AlH_3 in this system: on the anode side, Al^* and $LiAlH_4$/AlH_4^- species in the electrolyte synergistically participate in oxidative conversion, and the main reaction for AlH_3 formation is (1):

$$3LiAlH_4 + Al \rightarrow 4AlH_3 + 3Li^+ + 3e^- \quad (1)$$

On the cathode side, Li^+ and $LiAlH_4$ are reduced or participate in side reactions to maintain charge balance. The improved synthesis performance is attributed to the combined effects of Ni-enabled electronic conduction, interfacial electron redistribution, and the preservation of accessible Al reaction sites. These factors collectively alleviate passivation-induced charge-transfer limitation and enable sustained electrochemical formation of TEDA-trappable AlH_3 species.

Just Accepted

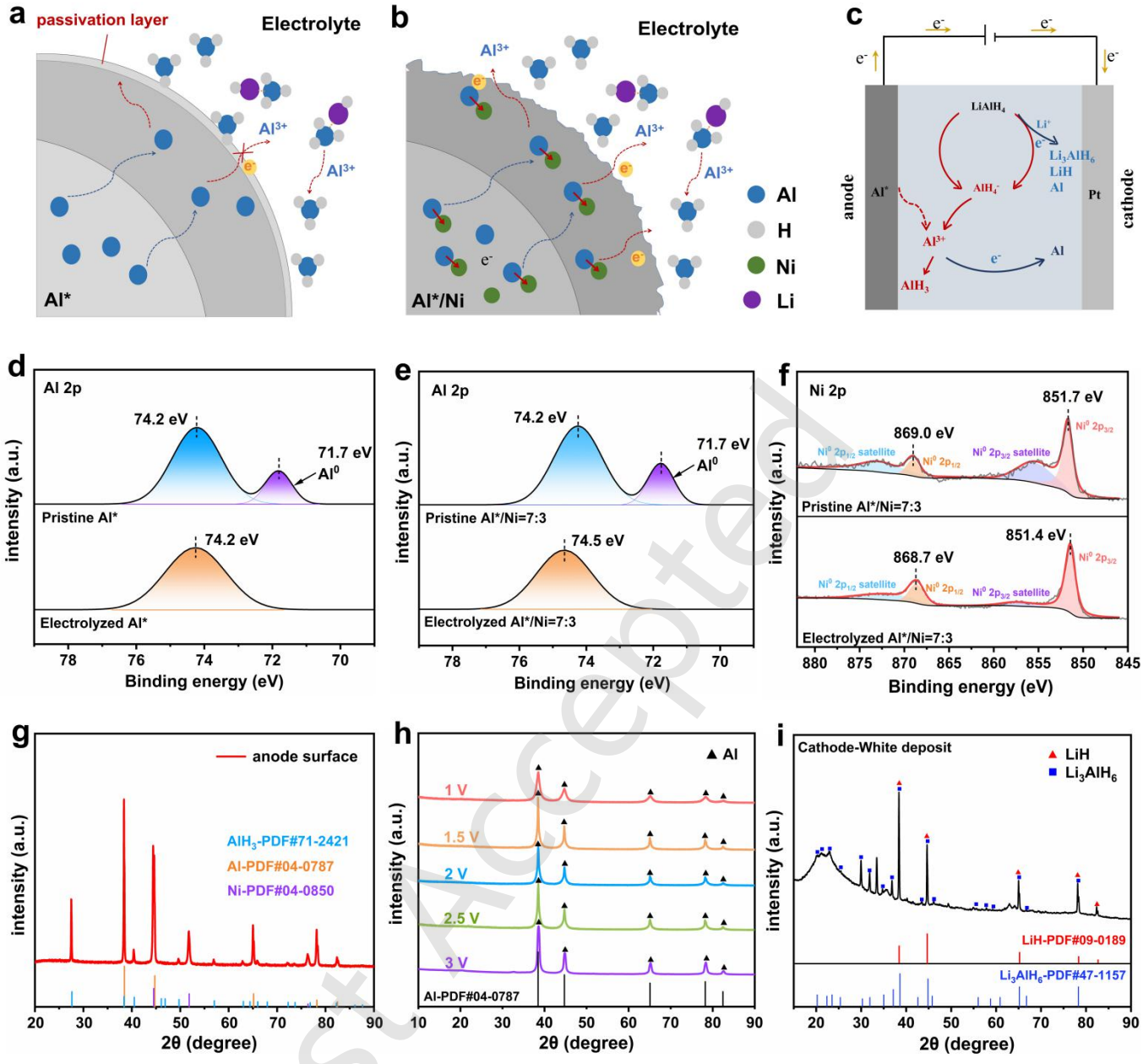


Figure 5. Analysis of the electrochemical reaction process. (a) Schematic illustration of electrolysis using Al* as the anode material. (b) Schematic illustration of electrolysis using Al*/Ni=7:3 as the anode material. (c) Proposed mechanism of the electrochemical reaction process; red and blue arrows represent the main reaction and side/cathodic reactions, respectively. (d) Al 2p XPS spectra of the Al* anode material before and after electrolysis. (e) Al 2p XPS spectra of the Al*/Ni anode material before and after electrolysis. (f) Ni 2p XPS spectra of the Al*/Ni anode material before and after electrolysis. (g) XRD pattern of the Al*/Ni anode material after electrolysis at 2 V vs. Ag/AgCl. (h) XRD patterns of cathodic products after electrolysis at different applied potentials. (i) XRD pattern of the white film formed on the cathode after electrolysis.

Just Accepted

3.5 Mechanistic Analysis

To elucidate the molecular-level origin of the enhanced AlH_4^- activation and electrochemical AlH_3 formation enabled by the Al*/Ni composite anode, density functional theory (DFT) calculations have been performed using Al* and Al*/Ni interfacial models. As shown in Figure 6a, charge-density-difference distributions could be observed after AlH_4^- adsorption on both surfaces, where the yellow and cyan regions represent electron accumulation and depletion respectively, revealing strong interactions between AlH_4^- and the model surfaces. Compared with the Al* model, the Al*/Ni interfacial model has exhibited more pronounced charge polarization near the Ni-containing region, certifying that Ni incorporation regulates the local electronic environment of neighboring Al sites. The density of states/projected density of states (DOS/PDOS) results have further demonstrated that Ni incorporation could provide additional Ni-derived states near the Fermi level and give rise to an overlap between Al- and Ni-related electronic states as interfacial electronic structure (Figure 6b). According to the XPS binding-energy changes, these calculations are consistent with interfacial electronic redistribution between Al- and Ni-rich regions.

The computed reaction pathway further testifies that the

Al^*/Ni interfacial environment facilitates AlH_4^- activation. As shown in Figure 6c, H transfer does not proceed through simple direct dissociation from AlH_4^-; instead, it involves an Al···H···(Al^*/Ni) transition-state configuration cooperatively stabilized by interfacial sites. This configuration weakens the original Al-H bond and stabilizes the H-transfer process, indicating that the Al^*/Ni interface acts not only as an electron-transport pathway but also as a local bonding regulator during AlH_4^- activation. The adsorption-energy results (Figure 6d) have demonstrated that the adsorption energies of AlH_4^- on the Al^*/Ni and Al^* models are -4.37 and -4.63 eV, respectively. The slightly weaker AlH_4^- adsorption on Al^*/Ni indicates that the promotional effect of Ni has not arisen from stronger initial adsorption, but from a more balanced adsorption strength that facilitates subsequent activation and conversion of adsorbed AlH_4^-.

In addition, the free-energy pathway further supports this interpretation as shown in Figure 6e. The activation barrier for AlH_4^- activation on Al^* is 0.53 eV, and the AlH_3^*+H^* final state is 0.38 eV higher than the initial state with an energetically unfavorable process. In contrast, on the Al^*/Ni interfacial model, the activation barrier decreases to 0.39 eV, and the final-state energy decreases to −0.23 eV, demonstrating that the Al^*/Ni interface lowers the kinetic barrier for AlH_4^- activation and stabilizes the AlH_3^*+H^* final state. Therefore, the enhanced performance of the Al^*/Ni anode could be attributed to interfacial electronic-structure modulation and reaction-pathway optimization rather than to a simple increase in AlH_4^- adsorption strength. The introduction of Ni promotes interfacial electronic redistribution and creates a polarized Al^*/Ni contact environment. This electronic modulation could improve interfacial charge transport, lower the calculated activation barrier for AlH_4^- activation, and stabilize the AlH_3^*+H^* final state in this work.

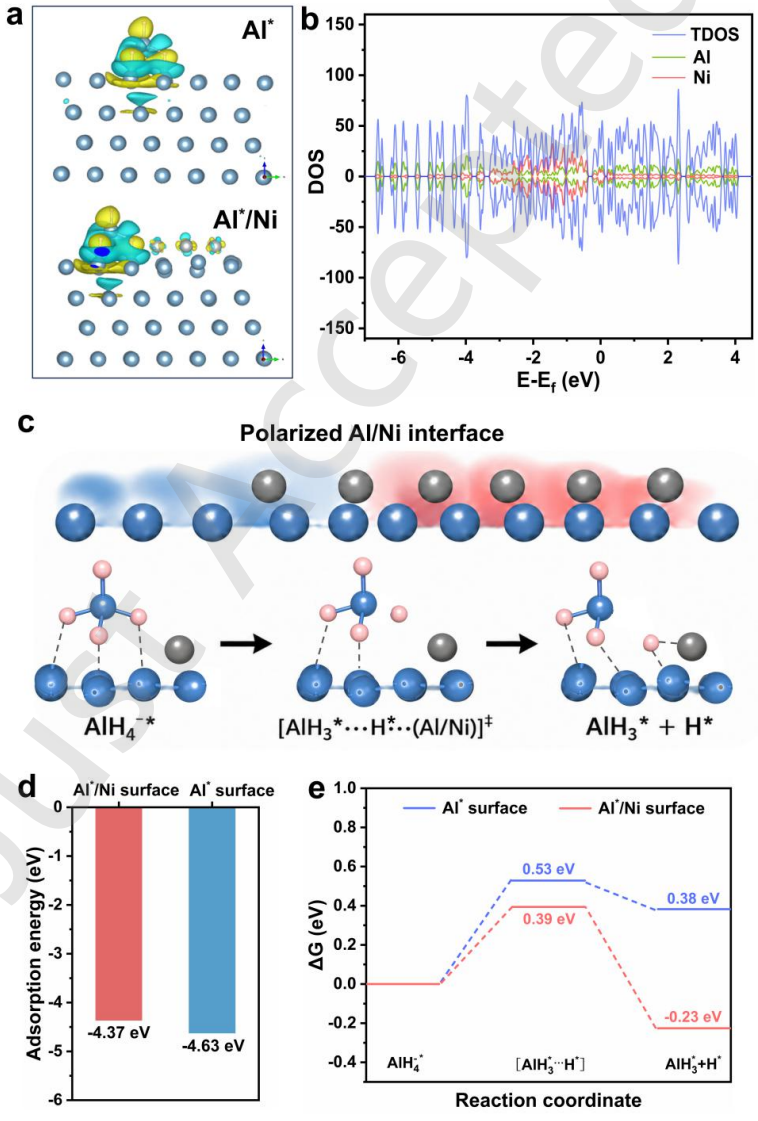


Figure 6. DFT analysis of AlH_4^- activation promoted by the Al^*/Ni surface. (a) Charge-density-difference maps after AlH_4^- adsorption on the Al^*/Ni and Al^* surfaces, where yellow and cyan represent electron accumulation and depletion regions, respectively. (b) DOS/PDOS profiles of the Al^*/Ni surface. (c) Schematic illustration of AlH_4^- activation promoted by the Al^*/Ni interface. (d) Comparison of AlH_4^- adsorption energies on the Al^*/Ni and Al^* surfaces. (e) Free-energy pathways for AlH_4^- activation on the Al^* and Al^*/Ni surfaces. Blue, gray, and pink spheres represent Al, Ni, and H atoms, respectively. The symbol ‡ denotes a transition state, whereas * denotes a surface adsorption site; a species followed by * represents its adsorbed state.

Just Accepted

4 Conclusions

In summary, a Ni-induced interfacial engineering strategy has been carried out to promote the electrochemical formation of AlH_3 from dehydrogenated aluminum in a $LiAlH_4$/THF electrolyte. The optimized Al^*/Ni=7:3 composite anode delivered a high current density of 0.123 A cm^{-2} at 2.0 V vs. Ag/AgCl, which is 2.7 times that of pristine Al^*, and retained 80% of its initial current after 3 h of operation, demonstrating long-term current stability. Under the optimized conditions, the AlH_3 formation rate reached 5.56 mmol h^{-1} with a Faradaic efficiency of 77.62%. Ni incorporation mitigated surface-layer accumulation and passivation-associated current decay, thereby helping preserve accessible Al reaction sites. The opposite shifts of the Al 2p and Ni 2p signals are consistent with interfacial charge redistribution and support the formation of a polarized Al/Ni interfacial environment. The calculated activation barrier for AlH_4^- conversion has been decreased from 0.53 eV on Al^* to 0.39 eV on the Al^*/Ni model, while the relative free energy of the AlH_3^*+H^* final state decreased from +0.38 to −0.23 eV. Therefore, this work has demonstrated a Ni-induced interfacial strategy for sustaining Al-participating electrochemical synthesis and presented a proof of concept toward electrically driven recycling of aluminum-based hydrogen carriers aiming at an advanced clean closed-loop energy route.

Data availability statement

The data supporting this article have been included as part of the main text and the Electronic Supplementary Information (ESI).

Electronic Supplementary Material:
Supplementary material (Figures S1–S12 and Tables S1–S2) is available in the online version of this article at https://doi.org/10.26599/NR.2026.94909297.

Acknowledgements

This work was jointly supported by the National Natural Science Foundation of China (22579001), the Key Research and Development Program of Jiangxi Province (20261BCG330001), the Anhui Provincial Natural Science Foundation (2408085ME106), and the Distinguished Young Scholars Research Project of Anhui Province (2022AH020013).

Declaration of competing interests

The authors declare that they have no known competing financial interests or personal relationships that could have appeared to influence the work reported in this paper.

Author contributions

Man Liu: conceptualization, methodology, investigation, data curation, formal analysis, visualization, and writing–original draft. Chunqi Zhang: conceptualization, methodology, investigation, data curation, formal analysis, validation, visualization, and writing–original draft. Licheng Liang: methodology, investigation, formal analysis, software, and visualization. Chuan Cao: methodology, investigation, validation, and writing–review & editing. Yichen Li: investigation, validation, and formal analysis. Mingan Ren: conceptualization, resources, and writing–review & editing. Ning Wang: methodology, software, formal analysis, data curation, visualization, and writing–original draft. Qingshuang Wang: investigation, formal analysis, validation, supervision, and writing–review & editing. Qingqing Yang: supervision, validation, and writing–review & editing. Fei Liang: conceptualization, supervision, resources, project administration, funding acquisition, and writing–review & editing.

Use of AI statement

None.

References

ADDIN EN.REFLIST [1] Galimova T, Ram M, Bogdanov D, Fasihi M, Gulagi A, Khalili S, et al. Global trading of renewable electricity-based fuels and chemicals to enhance the energy transition across all sectors towards sustainability. Renewable and Sustainable Energy Reviews. 2023;183.
[2] Hren R, Vujanović A, Van Fan Y, Klemeš JJ, Krajnc D, Čuček L. Hydrogen production, storage and transport for renewable energy and chemicals: An environmental footprint assessment. Renewable and Sustainable Energy Reviews. 2023;173.
[3] Klopčič N, Grimmer I, Winkler F, Sartory M, Trattner A. A review on metal hydride materials for hydrogen storage. Journal of Energy Storage. 2023;72.
[4] Wang Y, Xue Y, Züttel A. Nanoscale engineering of solid-state materials for boosting hydrogen storage. Chemical Society Reviews. 2024;53:972-1003.
[5] Yang M, Hunger R, Berrettoni S, Sprecher B, Wang B. A review of hydrogen storage and transport technologies. Clean Energy. 2023;7:190-216.
[6] Dematteis EM, Berti N, Cuevas F, Latroche M, Baricco M. Substitutional effects in TiFe for hydrogen storage: a comprehensive review. Materials Advances. 2021.
[7] Kumar N, Lee S-Y, Park S-J. Advancements in hydrogen storage technologies: A comprehensive review of materials, methods, and economic policy. Nano Today. 2024.
[8] Wang S, Li Z, Gao M, Liu Y, Pan H. Low-temperature and reversible hydrogen storage advances of light metal borohydrides. Renewable and Sustainable Energy Reviews. 2024.
[9] Xu Y, Zhou Y, Li Y, Hao Y, Wu P, Ding Z. Magnesium-Based Hydrogen Storage Alloys: Advances, Strategies, and Future Outlook for Clean Energy Applications. Molecules. 2024.
[10] Jiang W, Wang H, Zhu M. AlH3 as a hydrogen storage material: recent advances, prospects and challenges. Rare Metals. 2021;40:3337-56.
[11] Brower FM, Matzek NE, Reigler PF, Rinn HW, Roberts CB, Schmidt DL, et al. Preparation and properties of aluminum hydride. Journal of the American Chemical Society. 1976.
[12] Yao P, Zhao H, Zhang M, Xia C, Yang T, Li Q. Synthesis of α-AlH3 by organic liquid reduction method and its hydrogen desorption performance. International Journal of Hydrogen Energy. 2023.
[13] Lacina D, Reilly J, Celebi Y, Wegrzyn J, Johnson J, Graetz J. Regeneration of Aluminum Hydride Using Trimethylamine. The Journal of Physical Chemistry C. 2011;115:3789-93.
[14] M.J. Martínez-Rodríguez, B.L. García-Díaz, J.A. Teprovich, D.A. Knight, R. Zidan, Direct and reversible synthesis of AlH_3 - triethylenediamine from Al and H_2 , J. Phys. Chem. C 116 (2012) 23547–23552.
[15] J. Graetz, Y. Lee, A. Reilly, J. Wegrzyn, Location of Ti catalyst in the reversible AlH_3 adduct of triethylenediamine, J. Phys. Chem. C 115 (2011) 25209–25215.
[16] Zidan R, Garcia-Diaz BL, Fewox CS, Stowe AC, Gray JR, Harter AG. Aluminium hydride: a reversible material for hydrogen storage. Chem Commun (Camb). 2009:3717-9.
[17] Martínez-Rodríguez MJ, García-Díaz BL, Teprovich JA, Knight DA, Zidan R. Advances in the electrochemical regeneration of aluminum hydride. Applied Physics A. 2011;106:545-50.
[18] Do V-H, Lee J-M. Surface engineering for stable electrocatalysis. Chemical Society Reviews. 2024;53:2693-737.
[19] Shi H, Li Y, Pang S, Ma A, Lai J, Wang L. Electronic structure manipulation in electrocatalysis: mechanisms and design principles. Chemical Science. 2026.

Just Accepted

[20] Zhang Y, Lin Y, Duan T, Song L. Interfacial engineering of heterogeneous catalysts for electrocatalysis. Materials Today. 2021;48:115-34.
[21] Zhang Y, Nie K, Yi L, Li B, Yuan Y, Liu Z, et al. Recent Advances in Engineering of 2D Materials-Based Heterostructures for Electrochemical Energy Conversion. Advanced Science. 2023.
[22] Yang C, Gao Y, Ma T, Bai M, He C, Ren X, et al. Metal Alloys-Structured Electrocatalysts: Metal–Metal Interactions, Coordination Microenvironments, and Structural Property–Reactivity Relationships. Advanced Materials. 2023.
[23] Calle-Vallejo F, Tymoczko J, Colic V, Vu QH, Pohl MD, Morgenstern K, et al. Finding optimal surface sites on heterogeneous catalysts by counting nearest neighbors. Science. 2015.
[24] Park SH, To DT, Myung NV. A review of nickel-molybdenum based hydrogen evolution electrocatalysts from theory to experiment. Applied Catalysis A: General. 2022.
[25] Ortmeyer J, Bodach A, Sandig-Predzymirska L, Zibrowius B, Mertens F, Felderhoff M. Direct Hydrogenation of Aluminum via Stabilization with Triethylenediamine: A Mechanochemical Approach to Synthesize the Triethylenediamine · AlH(3) Adduct. Chemphyschem. 2019;20:1360-8.
[26] N.M. Alpatova, T.N. Dymova, Y.M. Kessler, O.R. Osipov, Physicochemical properties and structure of complex compounds of aluminium hydride, Russ. Chem. Rev. 37 (1968) 99–114.
[27] Wong BM, Lacina D, Nielsen IM, Graetz J, Allendorf MD. Thermochemistry of Alane Complexes for Hydrogen Storage: A Theoretical and Experimental Investigation. J Phys Chem C Nanomater Interfaces. 2011;115:7778-86.
[28] Lizarbe AJ, Major GH, Fernandez V, Fairley N, Linford MR. Insight note: X-ray photoelectron spectroscopy (XPS) peak fitting of the Al 2p peak from electrically isolated aluminum foil with an oxide layer. 2023;55:651-7.
[29] Zähr J, Oswald S, Türpe M, Ullrich HJ, Füssel U. Characterisation of oxide and hydroxide layers on technical aluminum materials using XPS. Vacuum. 2012.
[30] K. Hoang, A. Janotti, C.G. Van de Walle, Decomposition mechanism and the effects of metal additives on the kinetics of lithium alanate, Phys. Chem. Chem. Phys. 14 (2012) 2840–2848.
[31] Kresse, Furthmuller. Efficient iterative schemes for ab initio total-energy calculations using a plane-wave basis set. Physical Review B. 1996.
[32] Kresse G, Furthmüller J. Efficiency of ab-initio total energy calculations for metals and semiconductors using a plane-wave basis set. Computational Materials Science. 1996.
[33] Perdew JP, Burke K, Ernzerhof M. Generalized Gradient Approximation Made Simple. Physical Review Letters. 1996.
[34] Blöchl PE. Projector augmented-wave method. Physical Review B. 1994;50:17953-79.
[35] Kresse G, Joubert D. From ultrasoft pseudopotentials to the projector augmented-wave method. Physical Review B. 1999;59:1758-75

Just Accepted

Electronic Supplementary Material

Ni-induced interfacial engineering enables recycled aluminum hydride for high-efficiency electrochemical hydrogen storage

Man Liu [1], Chunqi Zhang [1], Licheng Liang [1], Chuan Cao [1], Yichen Li [4], Mingan Ren [4], Ning Wang [5], Qingshuang Wang [3] ✉, Qingqing Yang [2] ✉, Fei Liang [1] ✉

[1] Institutes of Physical Science and Information Technology, Anhui University, Hefei 230601, China
[2] School of Materials Science and Engineering, Anhui University, Hefei 230601, China
[3] School of Materials Science and Engineering, Changchun University of Science and Technology, Changchun 130022, China
[4] Henan Hydrogen Source Technology Co., Ltd., Xinxiang 453000, China
[5] School of Science, Key Laboratory of High Performance Scientific Computation, Xihua University, Chengdu 610039, China

Supporting information to https://doi.org/10.26599/NR.2026.94909297

Just Accepted

S1. Electrochemical measurements and electrochemical synthesis of AlH_3

A 1.0 M $LiAlH_4$/THF solution was used as the electrolyte. Cyclic voltammetry and linear sweep voltammetry were performed without iR compensation. Linear sweep voltammetry was conducted at a scan rate of 50 mV s^{-1}. Potentiostatic electrolysis was carried out at the specified applied potentials, with typical electrolysis conditions of 2.0 V vs. Ag/AgCl for 3 h. The 3 h chronoamperometric experiments were used to evaluate the current stability and passivation behavior of the anodes. Separate potentiostatic electrolysis experiments conducted for 1 h under otherwise identical conditions were used for quantitative determination of the AlH_3 formation rate and Faradaic efficiency. Unless otherwise stated, all potentials are reported versus the Ag/AgCl reference electrode and were not converted to the reversible hydrogen electrode or standard hydrogen electrode scales.

S2. TEDA trapping and non-Al-anode control experiment

After potentiostatic electrolysis, 20 mL of the electrolyte was collected and filtered to remove detached electrode particles and other insoluble solids. Excess TEDA was subsequently added to capture solvated AlH_3 and Al-H-containing species generated during electrolysis. A white precipitate gradually formed after TEDA addition. The solid was collected by centrifugation at 8500 rpm for 2 min, washed three times with equal volumes of anhydrous THF to remove residual $LiAlH_4$, uncoordinated TEDA, and soluble byproducts, and then dried under an Ar atmosphere. The resulting solid is referred to as the AlH_3-TEDA adduct.

Because H_2 was detected during electrolysis with the Al^*/Ni anode, direct anodic conversion of AlH_4^- was considered a possible parallel reaction pathway. To evaluate whether the $LiAlH_4$/THF electrolyte could independently generate TEDA-trappable AlH_3 in the absence of an Al-based anode, the Al^*/Ni working electrode was replaced with a glassy carbon electrode. The electrolyte concentration and volume, applied potential, electrolysis duration, counter and reference electrodes, and subsequent TEDA-trapping and product-isolation procedures were kept identical to those used for the Al^*/Ni system. LSV and potentiostatic measurements in the actual $LiAlH_4$/THF electrolyte revealed a relatively low but measurable anodic background current at this potential. After electrolysis, only slight turbidity was

Address correspondence to Fei Liang, fliang@ahu.edu.cn; Qingqing Yang, qqyang@ahu.edu.cn; Qingshuang Wang, wangqingshuang@163.com

observed upon TEDA addition, and insufficient solid could be recovered by centrifugation for further characterization. These observations suggest that, under the investigated conditions, direct electrochemical oxidation of the $LiAlH_4$/THF electrolyte does not readily yield recoverable AlH_3-TEDA in the absence of an Al-based anode. These results highlight the importance of the Al-based anode in obtaining recoverable AlH_3-TEDA and are consistent with the proposed Al^*-involving reaction pathway.

S3. Determination of the AlH_3 formation rate and Faradaic efficiency

The amount of AlH_3 was determined from the mass of the isolated AlH_3-TEDA adduct using the experimentally determined average composition of AlH_3·1.4TEDA. The AlH_3 formation rate was calculated from the amount of isolated AlH_3 divided by the corresponding electrolysis time and is therefore independent of the assumed electron stoichiometry of the reaction pathway.

The Faradaic efficiency was calculated on the basis of the predominant Al-participating anodic pathway. Control electrolysis using a glassy carbon anode under otherwise identical conditions suggested that direct electrochemical oxidation of the $LiAlH_4$/THF electrolyte does not readily yield recoverable AlH_3-TEDA in the absence of an Al-based anode, supporting the important role of the Al-based interface in effective AlH_3 formation. Accordingly, the formation of 1 mol of AlH_3 was taken to correspond to the transfer of 0.75 mol of electrons, and the total charge was obtained by integrating the current-time curve over the independent 1 h electrolysis period. The reported value therefore represents the Faradaic efficiency calculated on the basis of the experimentally supported Al-participating pathway, although minor contributions from direct AlH_4^- conversion and other competing reactions cannot be completely excluded.

Table S1. Textural parameters of the Al^* and Al^*/Ni=7:3 anodes after potentiostatic electrolysis at 2.0 V vs. Ag/AgCl for 3 h. Prior to the measurements, the samples were degassed under vacuum at 250 °C for 7 h to remove physically adsorbed species. The specific surface area was calculated using the Brunauer-Emmett-Teller (BET) method. The total pore volume was determined from the amount of N_2 adsorbed at a relative pressure (P/P_0) of approximately 0.99, and the pore-size distribution and average pore diameter were calculated from the adsorption branch using the Barrett-Joyner-Halenda (BJH) model.

Textural parameter	Al^*	Al^*/Ni=7:3
BET surface area ($m^2 \cdot g^{-1}$)	26.74	6.04
Total pore volume ($cm^3 \cdot g^{-1}$)	0.0320	0.0103
BJH pore size (nm)	5.01	10.24
Average pore size (nm)	4.79	6.83

Table S2. Gas chromatography data for the non-condensable gas evolved during the TPD measurement of the AlH_3-TEDA adduct and for the pure H_2 external standard.

Sample (1 mL)	t_r (min)	Peak area (μV·s)	H (mAU)	W (sec)
	0.26	1830050	254.21	10.1
	0.24	1839038	236.25	11.0
Gas Evolved	0.26	1661781	361.12	7.5

Just Accepted

	0.27	1668758	339.91	7.8
	0.27	1811227	369.96	7.9
	0.25	1742203	376.85	7.6
H_2 standard	0.25	7129724	646.37	17.0
	0.27	6982872	647.68	7.6

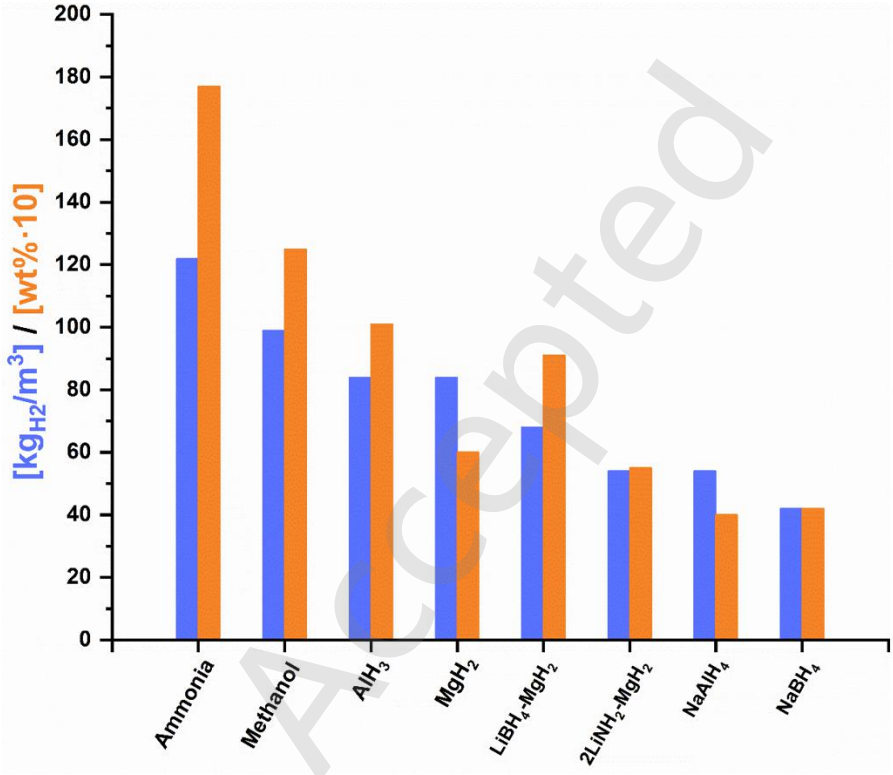


Figure S1. Eight hydrogen storage materials identified as having significant development potential by the U.S. Metal Hydride Center of Excellence (MHCoE).

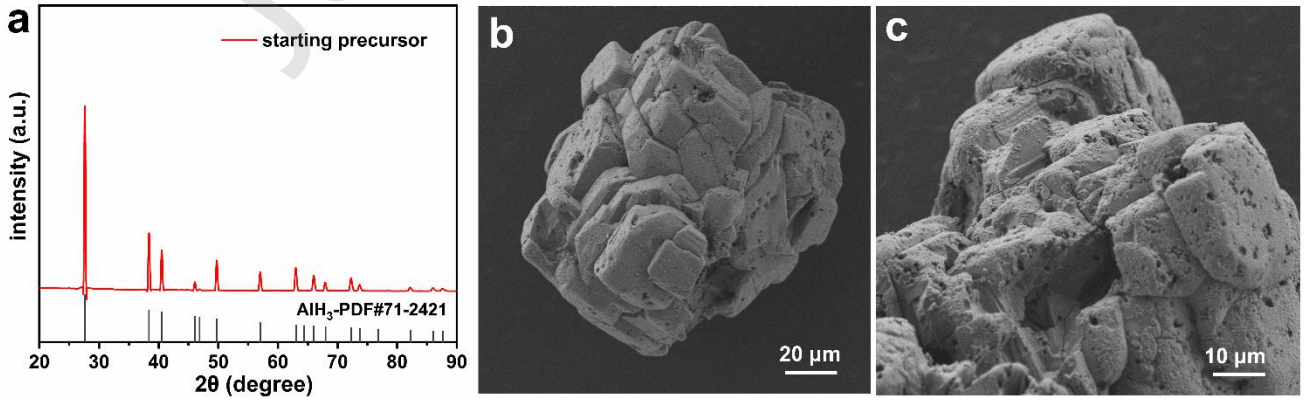


Figure S2. (a) XRD pattern, (b) SEM image, and (c) higher-magnification SEM image of the pristine α-AlH_3 precursor.

Just Accepted

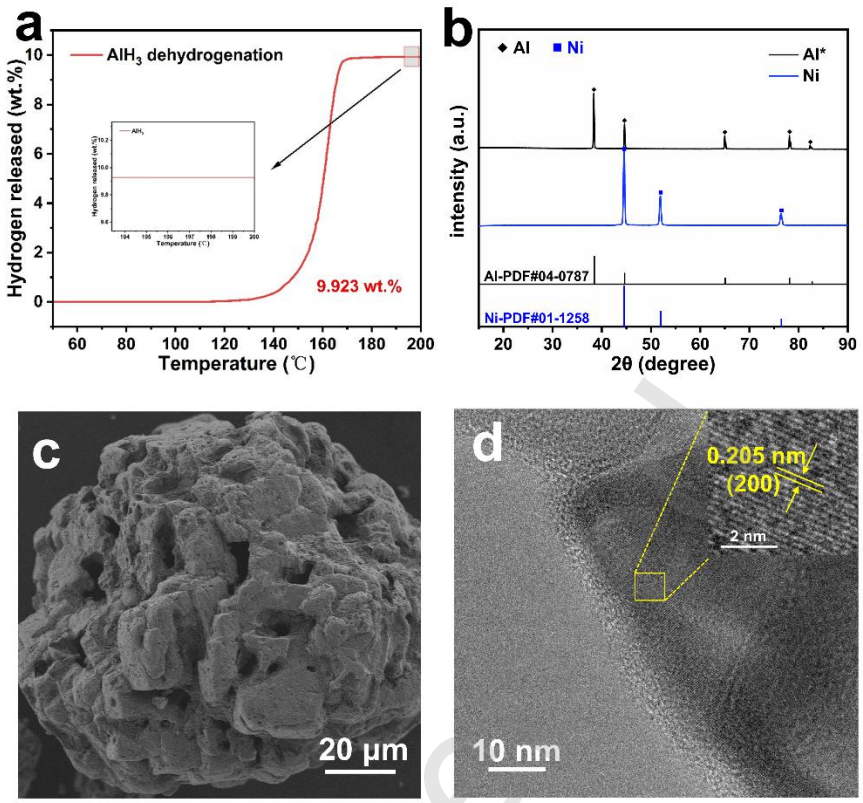


Figure S3. (a) Cumulative hydrogen release during temperature-programmed dehydrogenation of AlH_3. (b) XRD patterns of aluminum powder after temperature-programmed dehydrogenation of aluminum hydride and carbonyl nickel powder. (c) SEM image of Al^*. (d) HRTEM image of Al^*, showing a lattice spacing of 0.205 nm assigned to the Al (200) plane.

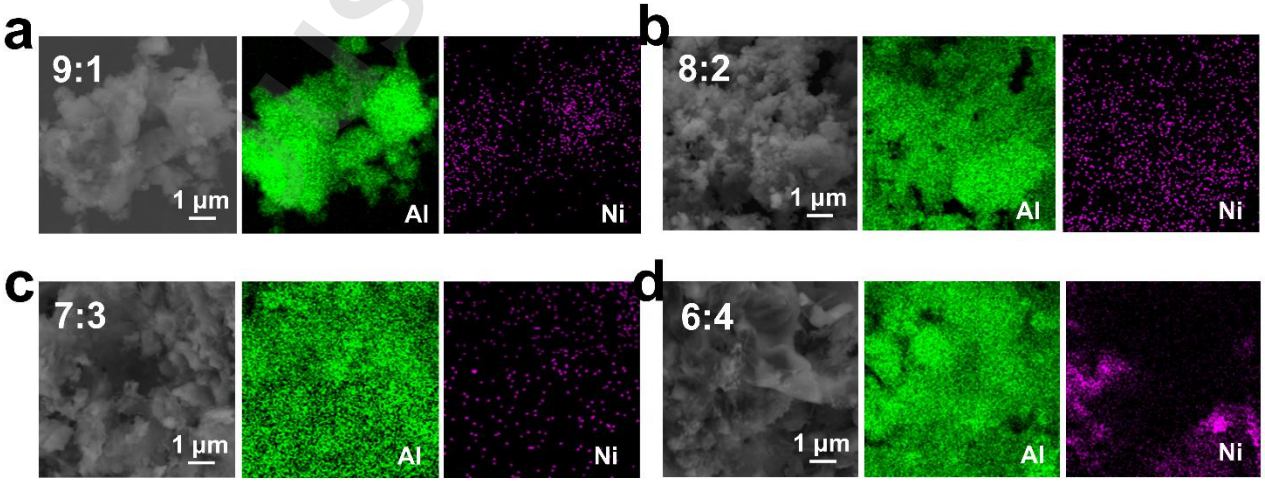


Figure S4. EDS images of Al^*/Ni anodes with different Ni contents after potentiostatic electrolysis. (a, b, c, d) Al^*/Ni ratios of 9:1, 8:2, 7:3, and 6:4, respectively. Potentiostatic electrolysis was performed at 2.0 V vs. Ag/AgCl for 3 h.

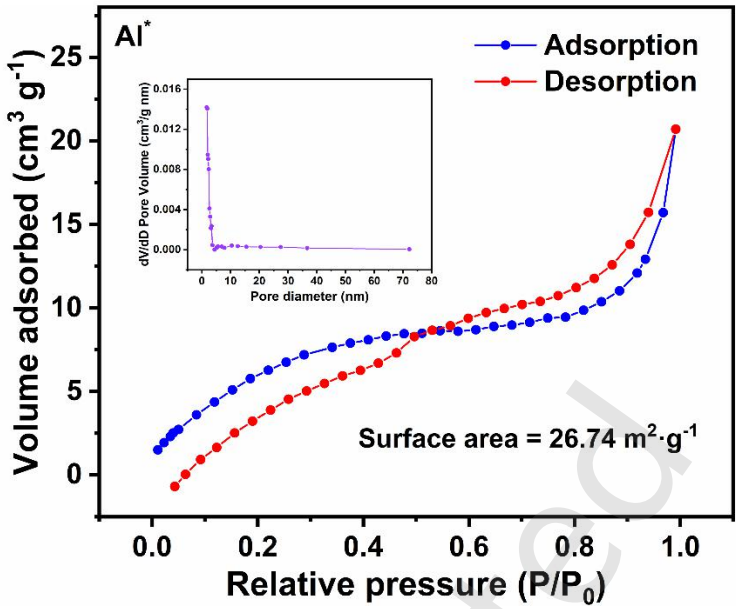


Figure S5. N_2 adsorption-desorption isotherm and corresponding pore-size distribution of the Al^* anode after potentiostatic electrolysis at 2.0 V vs. Ag/AgCl for 3 h.

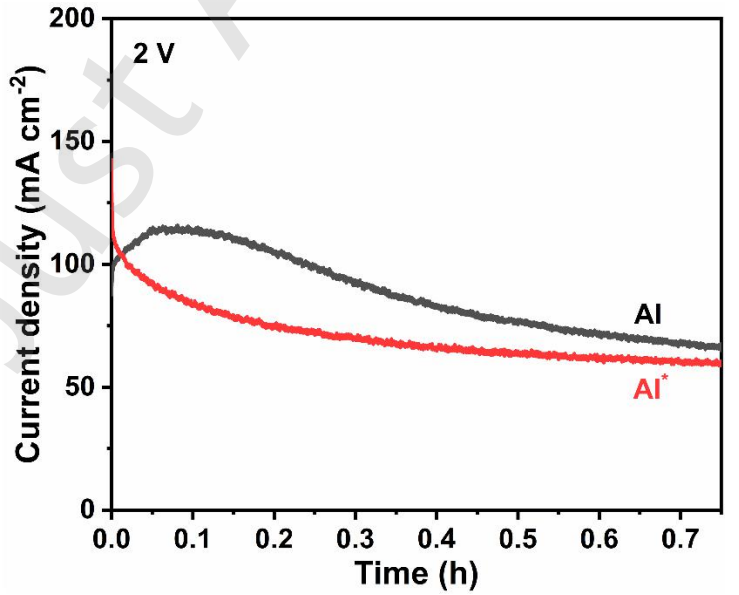


Figure S6. Current density-time (j-t) curves of electrolysis in a three-electrode system using commercial aluminum powder and highly active aluminum powder (Al^*) as anode materials. Potentiostatic electrolysis was performed at 2.0 V vs. Ag/AgCl for 45 min.

Just Accepted

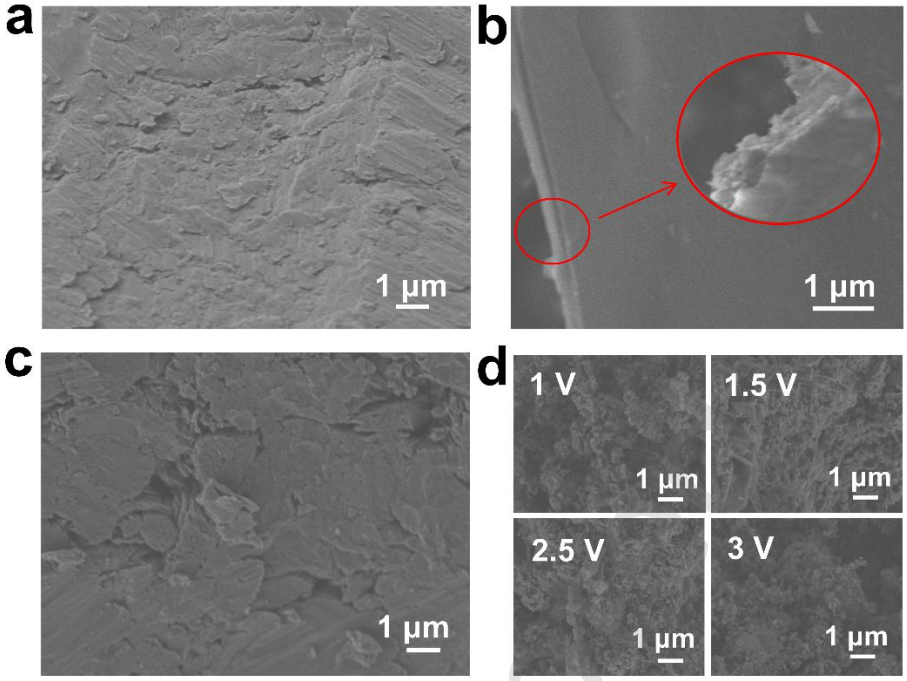


Figure S7. (a) SEM image of the pristine Al* anode. (b) SEM image of the Al* anode after potentiostatic electrolysis at 2.0 V vs. Ag/AgCl for 3 h. The red circles highlight the surface-covered region. (c) SEM image of the pristine Al*/Ni=7:3 anode. (d) SEM images of the Al*/Ni=7:3 anodes after potentiostatic electrolysis for 3 h at the applied potentials indicated in the individual panels. The Al*/Ni ratio is given on a mass basis.

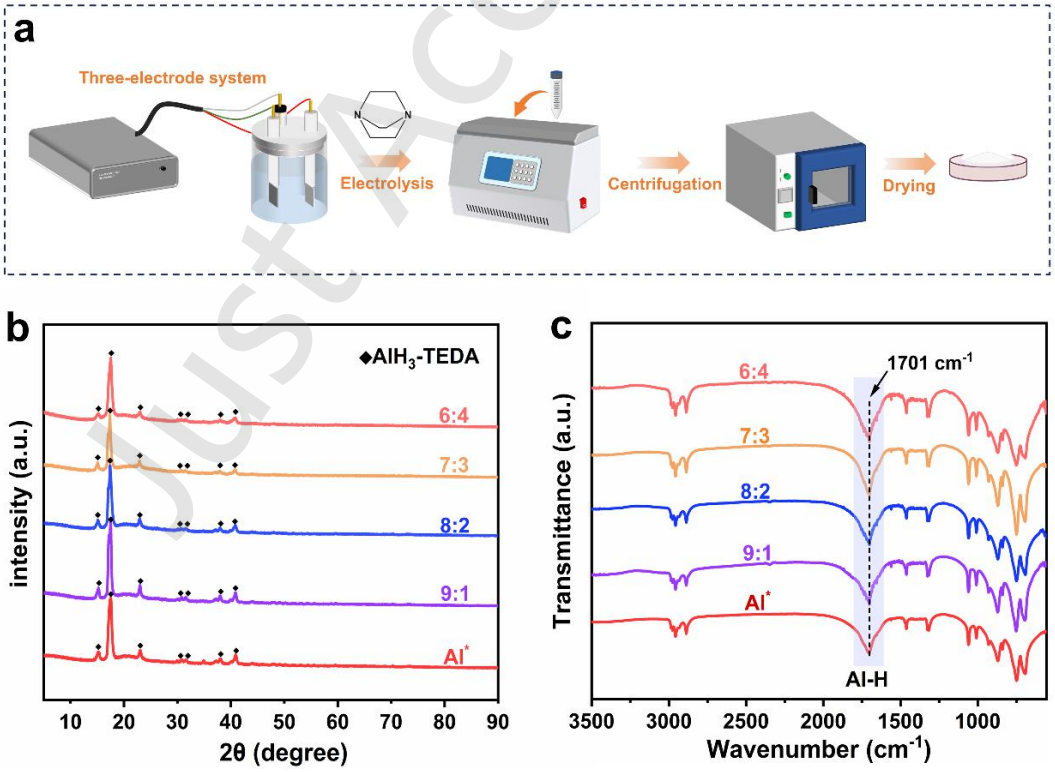


Figure S8. (a) Schematic illustration of the synthesis process of the AlH_3-TEDA adduct. (b) XRD patterns of AlH_3-TEDA with different Al*/Ni ratios as the anode materials. (c) FTIR spectra of AlH_3-TEDA with different Al*/Ni ratios as the anode materials. The AlH_3-TEDA products were obtained after potentiostatic electrolysis at 2.0 V vs. Ag/AgCl for 3 h.

Just Accepted

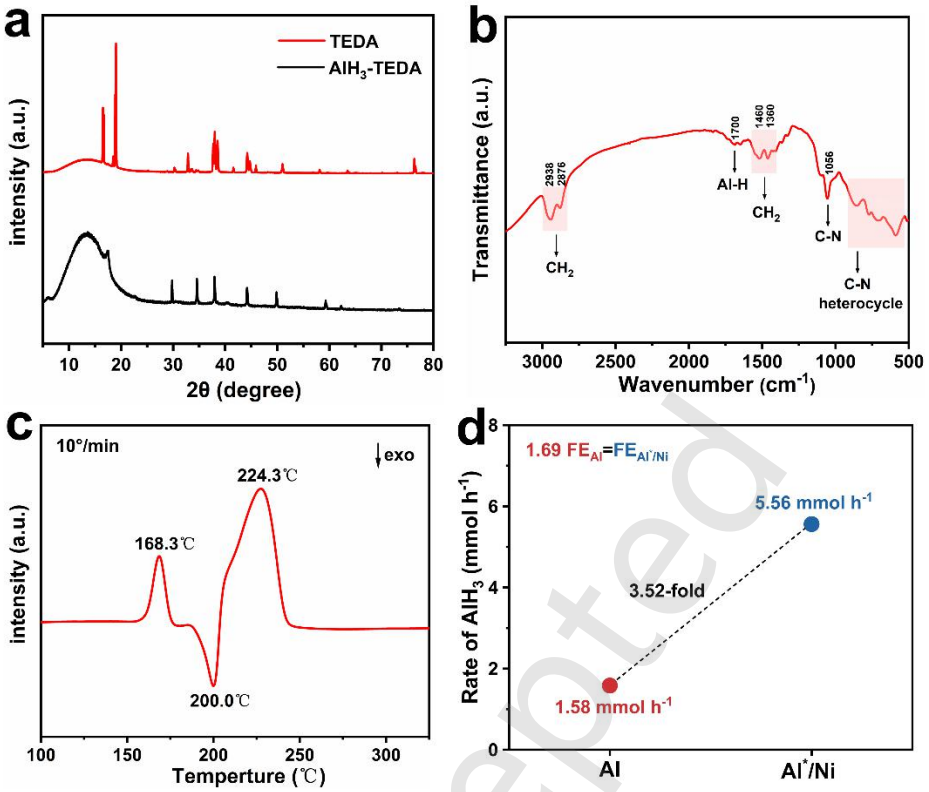


Figure S9. (a) XRD pattern, (b) FTIR spectrum, and (c) DSC curve of the isolated product obtained using commercial aluminum powder as the anode. The product was collected after potentiostatic electrolysis at 2.0 V vs. Ag/AgCl for 3 h. (d) Comparison of AlH_3 formation rates and the Faradaic efficiency ratio for commercial Al and Al*/Ni=7:3 anodes, determined from separate 1 h potentiostatic electrolysis experiments at 2.0 V vs. Ag/AgCl.

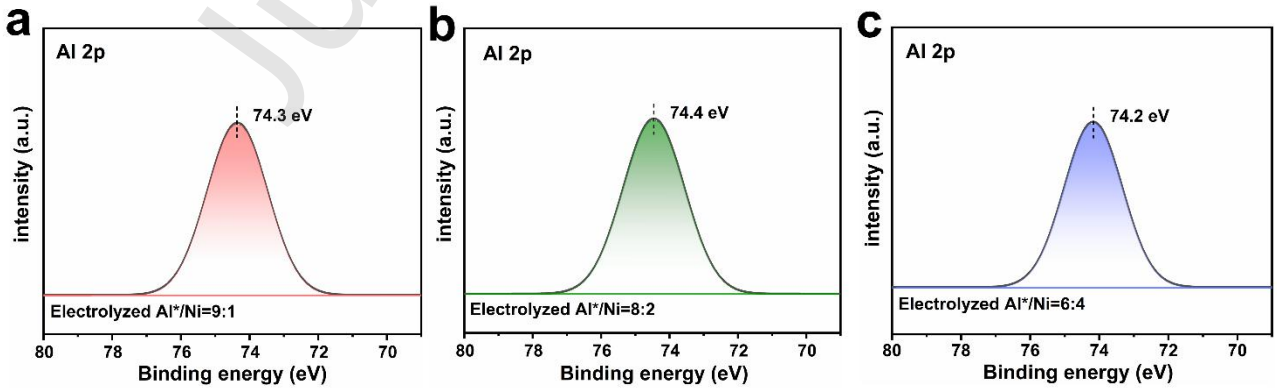


Figure S10. (a, b, c) Al 2p XPS spectra of the anode materials after electrolysis: Al*/Ni =9:1, 8:2 and 6:4. The anode samples were collected after potentiostatic electrolysis at 2.0 V vs. Ag/AgCl for 3 h.

Just Accepted

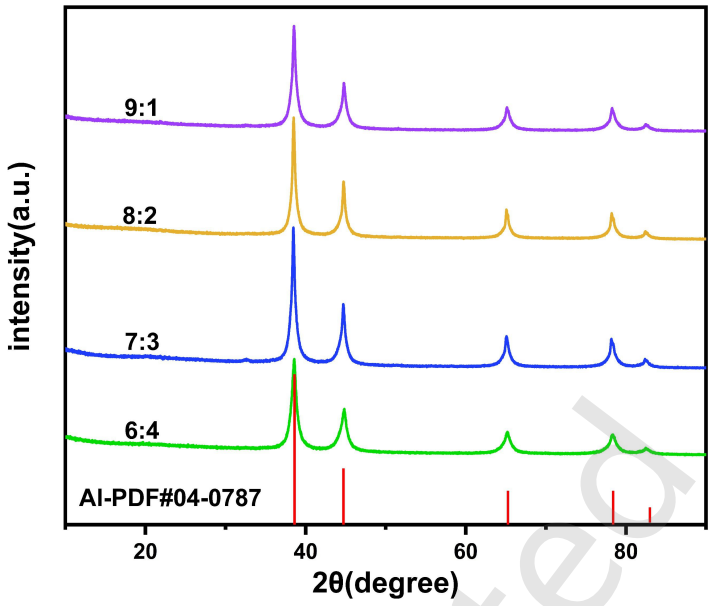


Figure S11. XRD patterns of the cathodic products obtained with different Al*/Ni ratios as the anode materials. The cathodic products were collected after potentiostatic electrolysis at 2.0 V vs. Ag/AgCl for 3 h.

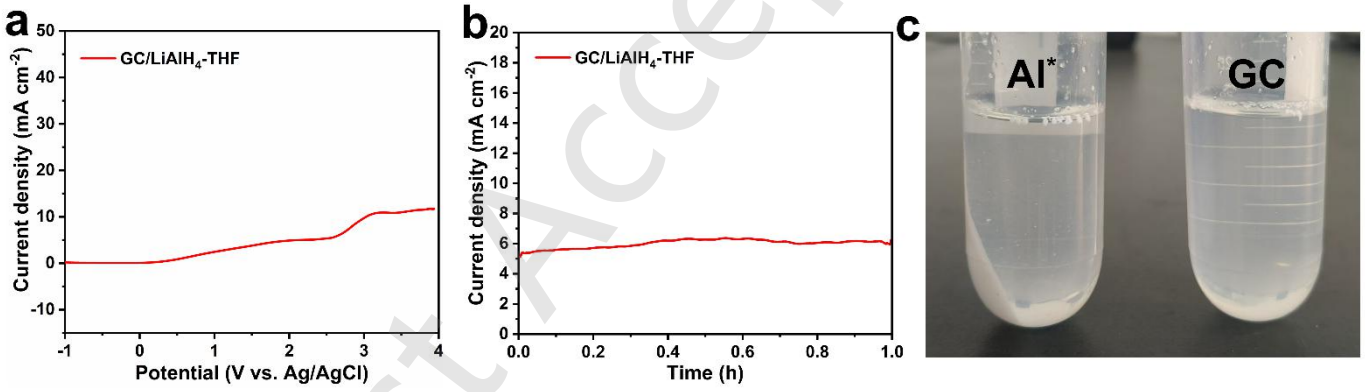


Figure S12. (a) LSV curve of a glassy carbon (GC) electrode in the $LiAlH_4$/THF electrolyte. (b) Current density-time curve recorded using the GC electrode during 1 h of potentiostatic electrolysis at 2.0 V vs. Ag/AgCl. (c) Photographs of the electrolytes after TEDA addition following electrolysis using Al* and GC anodes under identical conditions.

Just Accepted